行政院原子能委員會

委託研究計畫研究報告

創新加壓型固態氧化物燃料電池設計測試及模擬分析

Experimental and Numerical Simulation of Innovative Pressurized-Assembling Designs for Solid Oxide Fuel Cell

計畫編號：992001INER048

受委託機關(構)：國立中央大學

計畫主持人：施聖洋

核研所聯絡人員：李堅雄、胥耀華、柳輝忠

聯絡電話：03-4267327

E-mail address: sshy@ncu.edu.tw

報告日期：99 年 12 月

目　錄

中文摘要

本計畫以實作測試為主，輔以模擬分析，目標為建立一創新加壓型平板式固態氧化物燃料電池(SOFC)之實驗測試平台，以進行一系列高壓效應(1~5 大氣壓)對電池堆電池性能影響之實驗研究，所得結果將對未來發展高效率 SOFC 與氣渦輪機發電系統之整合技術有所幫助。本期計畫產出之成果有五項：(1)完成加壓型 SOFC 國際相關文獻之收集與彙整工作；(2)完成加壓型 SOFC 單電池堆實驗測試平台之設計與製作，除了測試高壓高溫實驗流程外，正進行一系列高壓高溫單電池堆性能測試實驗；(3)針對棋盤式流道尺寸效應，進行一系列單電池堆性能測試，找出棋盤式流道優化設計尺寸，將進一步執行高壓環境之測試；(4)建立密封材料之洩漏率測試平台，並針對新式壓縮密封材料進行洩漏率測試；(5)2010 年發表二篇國際 SCI 期刊論文(*J. Power Sources*)和四篇國際與國內會議論文。

關鍵字：加壓型平板式固態氧化物燃料電池、電池堆、壓力效應、棋盤式流道尺寸效應、電池性能測試平台

英文摘要

This project aims to establish an innovative pressurized platform for measurements and tests of the cell performance of planar solid oxide fuel cells (SOFC). Thus, a series of measurements of power generating characteristics for single-cell stacks at elevated pressures up to 5 atm can be performed. The obtained results should be of help to the future development of the high-efficiency SOFC and gas turbine integrating power generation technology. The followings are the project output including five items. (1) Complete high-pressure SOFC literature reviews. (2) Establish a platform for the test and measurement of high-pressure SOFC single-cell stacks. A series of cell performance measurement are currently conducted. (3) Study the scale effect of pin-type flow distributors on the cell performance of single-cell stacks for optimization. (4) Establish a platform for testing various sealing materials and measuring their leakage rates. (5) Publish two SCI journal papers (*J. Power Sources*) and four conference papers.

Key words: planar solid oxide fuel cell, stack, pressurized, scale effect, cell testing platform

壹、計畫緣起與目的

本計畫配合「新能源技術之發展與應用」計畫項下之「燃料電池發電」，分別利用實驗量測、數值模擬以及實作單電池堆性能測試，進行創新加壓型固態氧化物燃料電池(Solid Oxide Fuel Cell, SOFC)設計測試及模擬分析。

一、計畫緣起

化石燃料的迅速耗竭以及因溫室效應所造成的全球氣候變遷，是人們目前所面臨非常嚴峻的考驗，故世界各國皆以節能減碳作為在科技研發或政策制定方面的核心目標之一。

燃料電池藉由電化學反應直接將燃料之化學能轉換為電能，是一種高效率且潔淨的能量轉換裝置。在許多不同類型的燃料電池之中，固態氧化物燃料電池(solid oxide fuel cells, SOFC)具備許多的發展優勢，其中因 SOFC 可適用多種不同的燃料(含化石燃料與氫氣)，不僅可更有效率地使用化石燃料，也可將化石燃料直接轉換成電能、水蒸氣以及高純度的二氧化碳，有助於進行二氧化碳的捕捉與儲存，達到減碳的目標。因此，SOFC 被視為跨接現今碳氫經濟體系到未來氫經濟的重要能源載具之一[1]。此外，因為 SOFC 的操作溫度是所有燃料電池中最高溫(600 ~ 1000 oC)，適合結合淨煤技術以及氣渦輪機(gas turbine, GT)，並可視電力需求而發展成數百萬瓦等

級到數億瓦等級的定置型電力供應系統 [2]。台灣屬於高度仰賴進口能源的國家，若能積極發展以 SOFC 為主的發電技術，則不僅能提升我國的能源安全，並開創新興的高科技產業與就業機會，更能順應國際上節能減碳的趨勢。

我國核能研究所自 2003 年起開始著手研發平板式 SOFC 之發電技術，至今已獲得相當豐富的研究成果，含成功組裝測試 1 ~ 2 kW 級之 SOFC 電池堆，自行研製陽極支撐電池基板 (positive electrode-electrolyte-negative electrode, PEN)，設計製作燃料電池平衡系統(balance-of- plant)相關組件，並已建立用於預測電池性能與整體系統發電效率之數值模式[3-6]。而為了能將上述之成果的應用層面進一步擴展至 SOFC-GT 的複合式發電系統，核研所目前亦開始針對加壓式 SOFC 以及金屬支撐 PEN 等具前瞻性之議題進行研究。因此，本研究全力配合核研所的 SOFC 研發策略，針對(1)研發創新加壓型固態氧化物燃料電池(SOFC)之組裝技術，以及(2)流道尺寸效應對單電池堆性能之影響等兩大主題進行研究，期能建立氣體洩漏率之測試平台，協助核研所測試不同的高壓密封料與組裝技術，並藉由阻抗頻譜分析與數值模擬等基礎學理層面之電池性能劣化分析結果，進行流道尺寸之優化設計。本計畫所獲得之相關重要資料，應對於核研所未來擬進行之研究與電池堆設計有實質的幫助。

二、計畫目的

本計畫最主要目的是建立高壓式 SOFC 組裝技術研發與流道尺寸優化設計，並提出相關之研究成果，讓核研所進行系統改良時有可供參考之資料。本計畫二大主題的研究目的分述如下：

(一) 研發創新加壓型固態氧化物燃料電池(SOFC)的組裝技術

近年來，研發 SOFC-GT 複合式發電系統的相關研究相當受到矚目。然而，如何讓 SOFC 在高壓環境下穩定操作，使其尾氣可較容易與 GT 的操作條件契合，卻是仍待克服的關鍵技術。目前多種不同的電池堆設計中，美國 Siemens-Westinghouse 所開發的 tubular SOFC 以及 Rolls-Royce 所提出的 integrated planar SOFC，因其氣密性較佳，是兩種目前最常被應用於高壓式 SOFC 的設計[7,8]。而傳統的平板式 SOFC，如核研所目前研發中的雙進口/單出口設計，則較少相關文獻可供參考。為此，本計畫將進行完整的文獻回顧與分析，含(1)了解壓力效應對於電池性能以及電池操作壽命的影響；(2)由傳統機械設計以及熱交換器設計的文獻中，歸納出幾種可能適用於高壓式 SOFC 的組裝方式；以及(3)彙整多種用於平板式 SOFC 的密封材料與技術，其在不同壓力範圍之氣體洩漏率。此文獻回顧報告不僅對本研究後續進行的組裝技術研發有重大助益，也將可提供核研所開發金屬支撐 PEN 或新式密封材料相關的參考資料。此外，

我們也將嚐試建立氣體洩漏率測試平台，所擬建立的平台可於高溫高壓環境下操作，以執行本研究所需之實驗，未來並可配合核研所新開發密封材料，進行相關測試。

(二) 流道尺寸效應對單電池堆性能之影響

平板式 SOFC 流道設計方面的研究，可區分為流場均勻度的改良，以及流道尺寸優化設計兩大主要方向。本團隊過去致力於改善雙極板內部流場均勻度，已分別利用水力實驗模擬、數值模擬以及實際電池堆性能測試等方法，針對相關問題進行完整的測試分析，並提出一可使流場均勻與提升單電池堆性能的優化設計[9,10]。因此，本計畫主要針對流道尺寸對電池性能的影響，進行數值模擬與實驗測試。為了凸顯流道尺寸的效應，本研究擬以棋盤狀的流場板進行研究，並採用無因次寬度比 $f = w_{pin}/(w_{pin} + w_{channel})$來定義流道的特徵尺寸，其中 w_{pin} 與 $w_{channel}$ 分別為棋盤狀流場板上點狀凸出物的寬度以及流道寬度，故本實驗測試與數值模擬之結果，應也能應用於肋條式流道之設計。此外，因目前國際上與 SOFC 阻抗頻譜分析與量測的相關研究，多以鈕扣型 SOFC 操作於開迴路電壓(open circuit voltage, OCV)為對象，所獲得之結果並不適用於解釋流道尺寸效應所衍生的歐姆極化與濃度極化問題。因此，本研究將嚐試建立單電池堆操作於中高電流條件下的阻抗頻譜量測與分析技術，以量化流道尺寸效應對單電池堆性能之影響。

貳、研究方法與過程

本節將說明本計畫所採用之研究方法，包含研發創新加壓型固態氧化物燃料電池(SOFC)之組裝與實驗流程、密封材料洩漏率測試平台及測試分析流道尺寸效應對單電池堆性能之影響。

一、創新加壓型固態氧化物燃料電池實驗

本研究分為兩大部分(一)高壓型 SOFC 文獻回顧；(二)建立實驗平台與實驗程序。

(一)高壓型 SOFC 文獻回顧

SOFC 與 GT 的結合發電系統，可有效地提升系統整體的發電效率以及燃料使用率，是一種兼具經濟、環保與高效率的發電技術。若以 SOFC 電池堆的操作壓力對 SOFC-GT 複合發電系統進行分類，則有加壓式與常壓式兩種[11]。美國 Siemens-Westinghouse 是發展 SOFC-GT 複合發電系統的先驅，他們自 2000 年起，已建立許多不同發電規模，且以管狀 SOFC 電池堆為基礎的複合發電系統。在 Siemens-Westinghouse 目前已獲得的研究數據中，加壓式的複合發電系統可有較高的發電效率，以可將 SOFC 操作於約 7 bar 條件下的複合發電系統為例，當系統的發電規模為 2 百萬瓦以及 2 千萬瓦時，相對應的發電效率分別可達 60%與 70%，說明了加壓式複合發電系統的發展潛力[12、13]。正因加壓式 SOFC-GT 複合發電系統有如此

優異的性能，相關的研發工作正逐漸開始蓬勃發展，其中一部份的研究是以數值模擬或熱力學分析的方式，預測加壓式 SOFC 與 GT 的優化操作參數，如文獻[14-16]。而另一部份的研究則是分以美國 Siemens-Westinghouse 公司所建立的示範發電系統為例[15]，常壓型 SOFC-GT 系統中加壓的高溫空氣會經過熱交換器，先驅動 GT，然後再通入 SOFC。加壓型 SOFC-GT 系統則是將高壓高溫空氣先通入 SOFC，之後的尾氣再用來驅動 GT。由於 GT 的進口溫度會隨著壓力比增加而降低，故若採用高壓力比的 GT 設計，則加壓型 SOFC 將可有效改善進口溫度降低的問題，進而提升整體效率。

數值模擬方面，Ni et al. [17]以 Bulter-Volmer equation、Fick's law 以及 Ohmic law 建立一維的 SOFC 數值模式，並預測可具最佳電池性能的優化電極微結構以及優化操作條件。此研究所探討的操作壓力範圍為 0.5 bar ~ 5 bar，其結果顯示增加操作壓力有助於提升反應物的擴散率，而這不僅使電極觸媒的表面可完全與反應物接觸，降低活化極化，同時也可加快多孔電極內反應物與生成物的交換，進而抑制濃度極化現象。Patcharavorachot et al. [18]進一步修改 Ni et al. [17]的數值模式，將用於描述 SOFC 活化極化的 Bulter-Volmer equation 由原來的線性表示法改為非線性表示法，即交換電流密度(exchange current density)需由電化學反應率之指數前置因子(pre-exponential factor)以及反應物活化能(activation energy)求得，而

非一常數。經過修改後的數值模擬結果發現[18]，增加 SOFC 的操作壓力可明顯抑制濃度極化，但對活化極化的影響則相當不明顯。Bo et al. [19]不僅建立與前二者相似之數值模式，探討壓力效應對電池性能極化現象的影響，也利用 Aspen Plus 軟體分析 SOFC 在高壓條件下之發電效率。Bo et al. [19]的結果與 Ni et al. [17]相同，歸納出陽極的活化過電位及濃度過電位，隨操作壓力增加而下降原因：(1)操作壓力增加，則氣體濃度增加；(2)壓力增加，則氣體莫耳擴散率增加，因此有較低的濃度過電位；(3)壓力增加，在燃氣高莫耳濃度環境下，多孔性電極變得活躍，因此有較低活化過電位。但若要增加 SOFC 的操作壓力，則系統需要額外裝置一壓縮機，而壓縮機的耗能會降低 SOFC 發電系統的效率，故 SOFC 發電系統若操作於 1.33 atm，可獲得最佳的發電效率。

實驗測試方面，美國 Honeywell 曾於 2001 年受美國能源部委託，建立實驗室規模的加壓式平板型 SOFC 單電池堆測試平台，並測試 1 ~ 2 atm 條件下的電池性能[20]。實驗結果顯示，當操作溫度為 800^{o}C，且操作電壓為 0.6 V 時，常壓條件下之單電池堆開始產生濃度極化，而加壓式 SOFC 則未有濃度極化現象產生。此外，兩者於操作電壓為 0.6 V 時的功率密度約相差 100 mW/cm^{2}。Zhou et al. [21]以管狀 SOFC 單電池堆進行實驗測試，並由熱力學與化學反應動力學討論壓力效應與溫度效應何者為主導電池性能之要素。結果顯

示，增加操作溫度在熱力學上屬於負面的影響(降低 OCV)，但在化學反應動力學方面則為正面影響(增加反應率)；增加操作溫度則對兩方面都屬於正面影響，故壓力效應為主導電池性能變化的因素，且性能隨壓力增加而增加。Thomsen et al. [22]以阻抗頻譜量測的方式，研究壓力效應對鈕扣型 SOFC 氧離子傳輸機制的影響。他們發現，增加 SOFC 的操作壓力，可有助於改善陰極氧原子的吸附作用與離子的傳輸反應，而這對改善活化極化與歐姆極化都能有所幫助。

最近，Lim et al. [23]則以德國能源研究中心(Forschungszentrum Juelich, FZJ)所開發的 F-design 平板型 SOFC 為基礎，建立加壓式 40-cell stack，並將其與微氣渦輪機結合。他們首先獨立測試加壓式 SOFC 電池堆於不同壓力條件下(1 atm ~ 3.5 atm)之性能，結果發現，當操作電壓固定於 30 V 時，壓力若由 1 atm 增加至 2 atm，則功率密度增加約 4.2%。而壓力由 2 atm 增加至 3.5 atm 時，功率密度的增加率則低於 1%。雖然他們已成功將 FZJ 所開發的平板型 SOFC 操作於高壓條件中，並成功與微氣渦輪機結合建立 5 kW 等級的複合發電系統。但作者於論文中特別強調，此類型的電池堆在高壓環境下所造成的氣體洩漏問題仍未有效克服，且壓力爐與電池堆之間的壓力差不可大於 200 mbar，而多次實驗都因氣體洩漏或電池片破裂而失敗，且成功發電的複合發電系統在操作 1000 小時之後也會有明顯

的劣化率。核研所目前所採用的電池堆設計就是和 FZJ 相似的雙進口單出口流場板，因此未來建構 SOFC-GT 複合發電系統時，同樣會遭遇高壓條件下的氣體洩漏問題。

(二)建立實驗平台與實驗程序

如圖 2.1 左所示，高壓單電池堆性能測試平台包含五大項：(1)控制系統，利用電腦控制反應氣體之流量計以及預熱用的加熱線圈；(2)氣體供應系統，含氫氣、甲烷、丙烷、氮氣以及空氣之供應與相關管線及安全防爆閥等；(3)高壓高溫容器，包括加壓系統與溫度控制系統，壓力最高可加壓至 10 大氣壓。而溫度控制系統，含高溫爐與可程式化之控制器，最小升降溫速率可達 0.5 ^{o}C/min，最高操作溫度達 1200^{o}C；(4)量測系統，含電子負載儀和交流阻抗儀，交流阻抗儀之操作電流範圍為 0 ~ 10 A，故可量測分析單電池堆之阻抗頻譜。

圖 2.1 右為置於高壓容器高溫爐內加壓單電池堆實驗測試組裝示意圖。我們使用陶瓷材料加工製成多種不同設計可重複使用之流場板，可避免因使用金屬雙極板所造成的鉻毒化問題。有關單電池堆各元件組裝說明，可見參考文獻 [24]。圖 2.1 右中上半部的彎管設計，是為了讓單電池堆不會受到管路因熱膨脹所造成之高溫應力之影響。

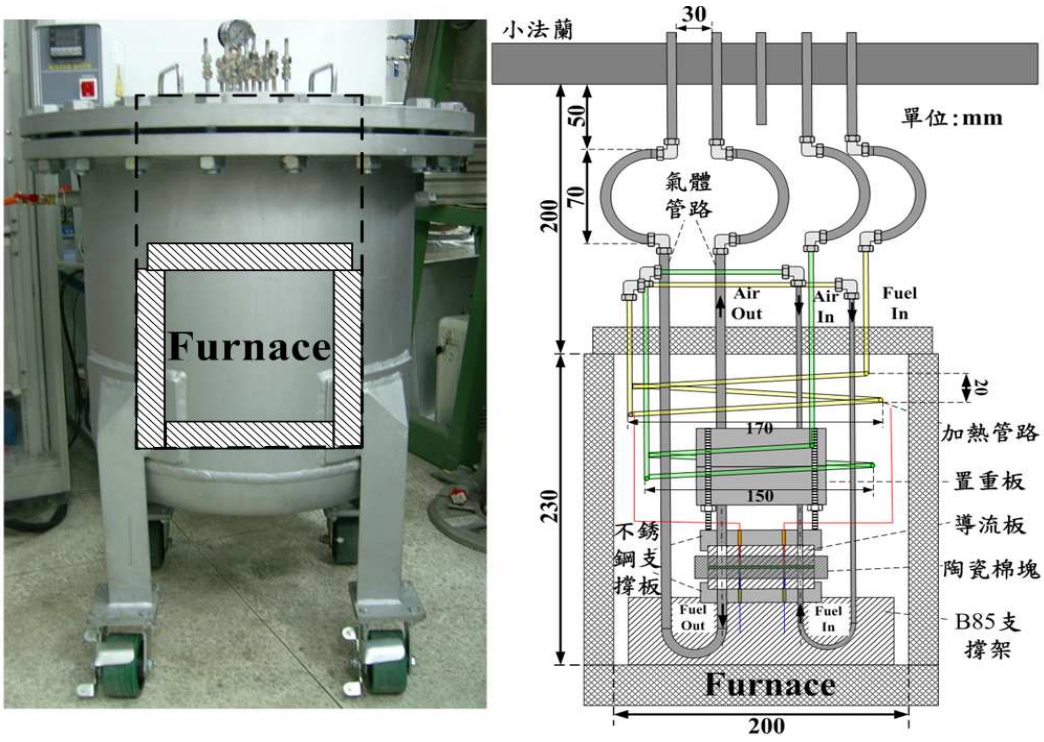

圖 2.1 左為高壓單電池堆測試容器，內含高溫爐及相關管路和壓力計等組件；右為高溫爐內加壓單電池堆測試組裝示意圖。

二、密封材料洩漏率實驗

圖 2.2 左邊為我們建立的洩漏率量測實驗平台，組件含不鏽鋼 SS316 製作的測試元件、氣體容器、質流量計、壓力計以及洩壓閥。測試元件的下板有一氣體腔室，用以模擬實際電池堆之洩漏率量測。實驗進行時，洩漏率量測公式：$L=(P_i-P_f)V/(P_f*t*C)$[25]，其中 L 為氣體洩漏率(sccm/cm)、V 為外部氣體容器的體積(cm^3)、P 為氣體壓力(Kgf/cm^2)、t 為時間(min)、C 為密封材料之周長(cm)、下標 i 與 f 則表示初始值與最終值。

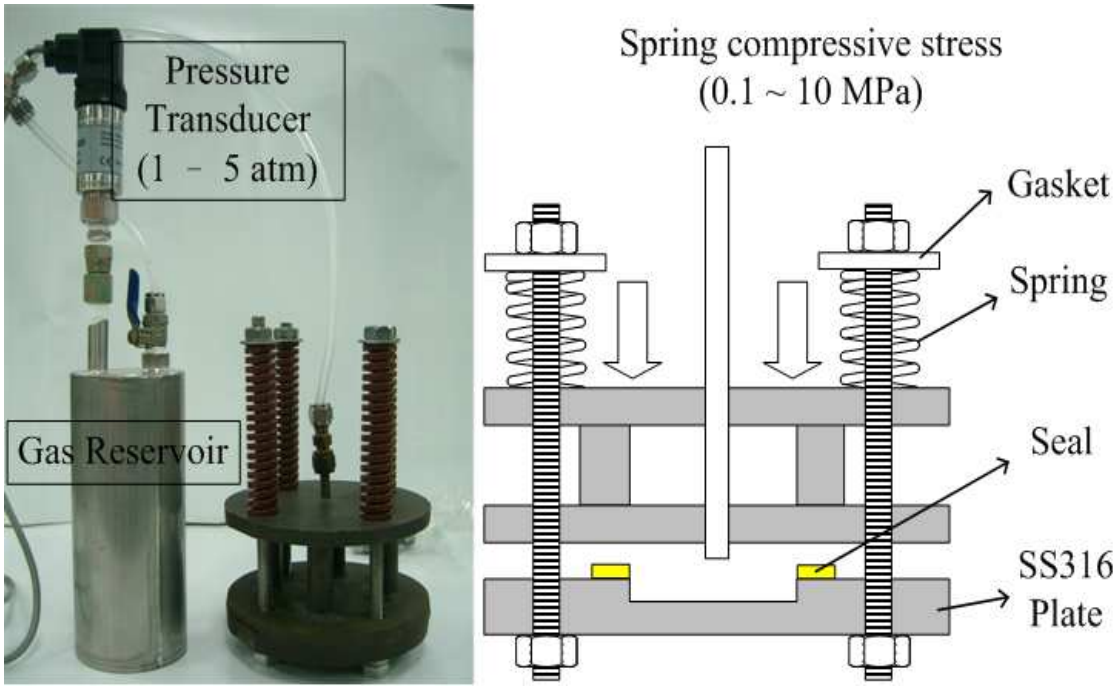

圖 2.2 左為氣體洩漏率測試平台及相關組件;右為測試平台示意圖。

三、尺寸效應對單電池堆性能量測實驗

單電池堆包含:PEN、雙極連接板、陶瓷外罩(ceramic housing)、上下金屬板(upper plate & bottom plate)，以及置重塊(load plate)，這些關鍵組件採無密封方式組裝，逐一在高溫爐內部堆疊組合，設備的示意圖與實際照片請見下圖 2.3。棋盤式流道雙極連接板採用熱膨脹係數與 PEN 相近的 Crofer-22-APU 金屬材料，可同時作為電子導電與反應氣體導流之用，兩端電極之雙極板分別焊接八條導線，同一端電極取四條作為電壓導線，另四條則作為電流導線。陽極端使用鎳作為導線，而陰極端則使用白金材料作為導線。陶瓷外罩採用耐高溫陶瓷材料 B85 來製作，B85 導電率低且具有相當抗壓強度，

因此置於雙極板與上下金屬板之間，作為絕緣與支撐之用。金屬板與置重塊以 SS316 不銹鋼材料製作，金屬板的主要用途在於焊接氣體管路，並達到單電池堆定位之用。置重塊放置於單電池堆上方，可提供總約 3 kg 的重力負載，使雙極板可以更緊密接觸 PEN。詳細的實驗條件與實驗過程，請參考本團隊李信宏先生之碩士論文[26]。

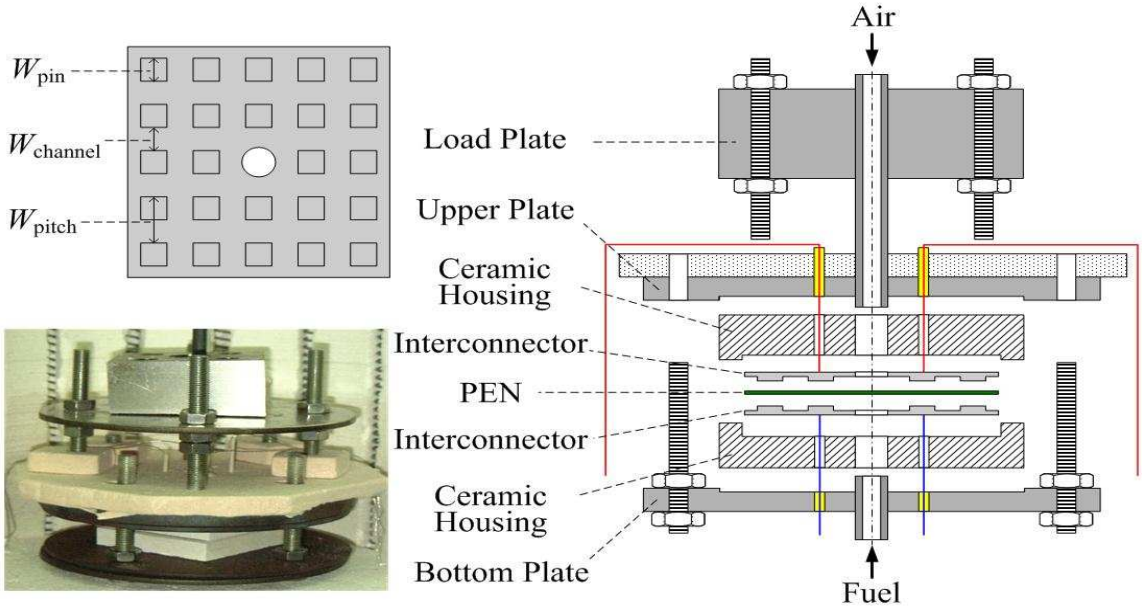

圖 2.3 單電池堆組裝後於高溫爐內實際圖片(左下)、棋盤式流道尺寸參數定義(左上)和單電池堆細部示意圖。

參、主要發現與結論

本節彙整本計畫所獲得的研究成果，最後做總結並規劃未來擬持續進行之研究工作。

一、結果與討論

以下說明本計畫所獲得之研究成果及主要發現，包含(1)高壓

SOFC 測試平台建立；(2)密封材料洩漏率測試；與(3) Pin-type 尺寸效應對單電池堆性能之影響。

(一)高壓 SOFC 測試平台建立

在本實驗室過去所累積之經驗[10]下，我們正建立加壓型單電池堆測試之標準實驗流程。針對高壓實驗流程進行測試，當高壓容器內之高溫爐升溫至 750 ℃時，高壓容器的外壁溫度約有 55 ℃左右。此測試目的在確認升壓速率對電池片的影響，故將升壓速率設定至兩大氣壓並固定此壓力，半小時後再降回常壓並降溫。升、降溫速率都為 1 ℃/min。實驗結果發現電池片破裂且電池片的支撐板(Frame)也產生形變。推測原因是升壓速率過快，0.15 atm/min 的升壓速率換算約有 20 L/min 的加壓氣體進入電池堆與高壓高溫容器內部，此加壓流量應仍太大。改善方式：以常壓型的實驗設備為基礎重新設計加壓實驗設備，並用置重的方式對電池堆施壓，這樣的設計可讓電池堆在熱膨脹時有收縮的空間，避免電池片受擠壓而破裂。在燃料與空氣入口管路加入瑞士捲加熱器，其目的是加熱管路內的氣體，避免氣體與電池片之間的溫差過大。也將升壓速率調整為 0.05 atm/min 換算約 7 L/min 的加壓氣體填入高溫高壓容器，目的是為了延長氣體的加熱時間。

(二)密封材料洩漏率測試

本實驗首先針對新式壓縮密封材料陶瓷纖維紙的製備程序進行優化：(1)首先烘烤，溫度需達 700 ^{o}C 並持續烘烤 1 小時，以去除纖維紙內部的有機雜質；(2)纖維紙浸泡二氧化矽水溶液時必須持續搖晃浸泡容器，以使二氧化矽水溶液充份滲入纖維紙內部，本實驗優化二氧化矽水溶液濃度為 150 g/L；(3)於溫度 160^{o}C 下烘燥 5 小時，蒸發水溶液水分使二氧化矽結晶附著於纖維紙孔隙；(4)纖維紙預壓可使二氧化矽結晶能更緊密地填滿纖維孔隙，本實驗優化預壓壓力為 6 Mpa。密封材料經優化製備後，即進行洩漏率測試，比較平台內外壓力梯度對洩漏率之影響。測試結果顯示，當壓應力為 6 Mpa，於 15 kpa 壓力梯度下洩漏率為 0.01 sccm/cm，而在 10 kpa 壓力梯度下洩漏率僅約 0.006 sccm/cm，顯示電池堆使用此種陶瓷纖維複合材料作為密封時，電池堆內部與外部之壓力梯度不宜超過 10 kpa。

(三)Pin-type 尺寸效應對單電池堆性能之影響

本研究雙極板共設計五組流道尺寸設計如圖 3.1 所示，實驗參數包含(1)3 種 W_{pitch} 值：固定 f 值為 0.5，W_{pitch} 值分別為 4 mm、6 mm、10 mm，其有效接觸面積比定義為 pin 總面積(A_{pin})與雙極板總面積(A_t)的比值(A_{pin}/A_t)，分別為 26%、22%及 24%；(2)3 種 f 值：固定 W_{pitch} 值為 4 mm，f 值分別為 0.33、0.5、0.66，有效接觸面積比(A_{pin}/A_t)分

別為 11%、26%及 45%。藉由採用這些不同流道尺寸的雙極板，於相同實驗操作條件下，即可探討流道尺寸效應對單電池性能的影響。

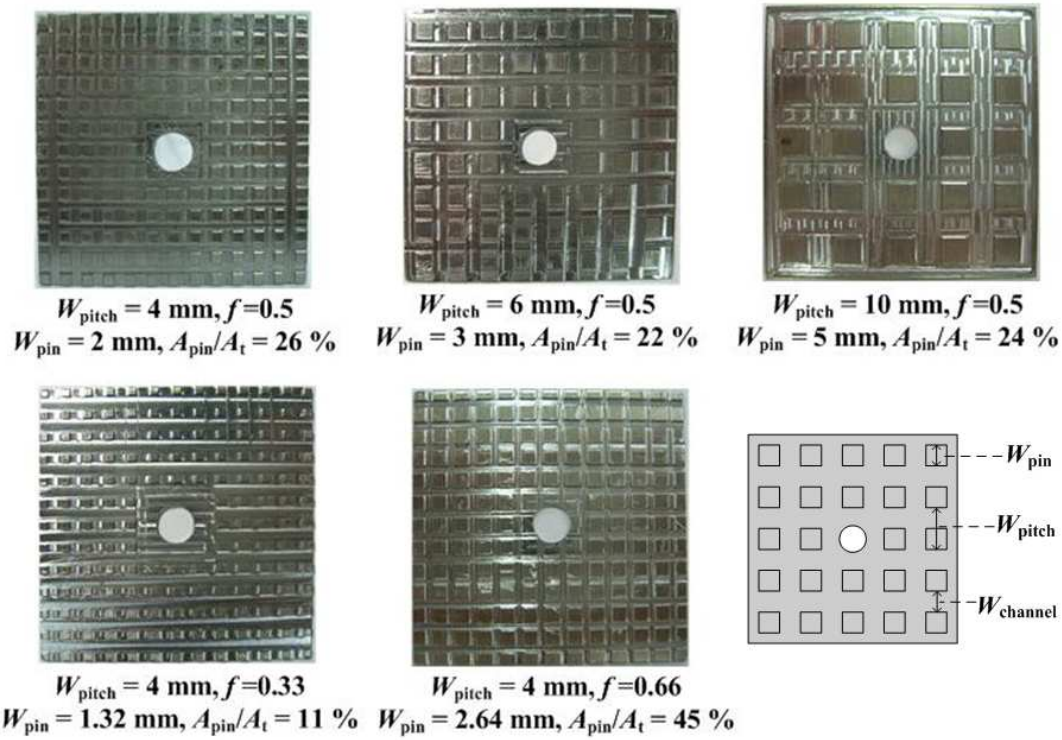

圖 3.1 不同尺寸設計的棋盤式流道。

首先固定 f 值為 0.5，探討 W_{pitch} 值分別為 4 mm、6 mm，以及 10 mm 時，電池性能的差異，此三種尺寸設計代表 pin 及流道的寬度各為 2 mm、3 mm，以及 5mm，而 pin 與電極的有效接觸面積比則相當接近，約為 24 %。

極化曲線量測結果如圖 3.2 所示。可以發現，電池輸出功率隨 W_{pitch} 值減少而上升，當 W_{pitch} 值分別為 4 mm 與 10 mm 時，MPD 可相差 11%，而 ASR 隨 W_{pitch} 值減少而減少，於操作電壓 0.6 V 下，局部 ASR 可相差 25 %。此外，亦可發現 W_{pitch} = 4 mm 與 6 mm 的

MPD 或 ASR 都非常接近，顯示兩者的極化損失可能非常相近。

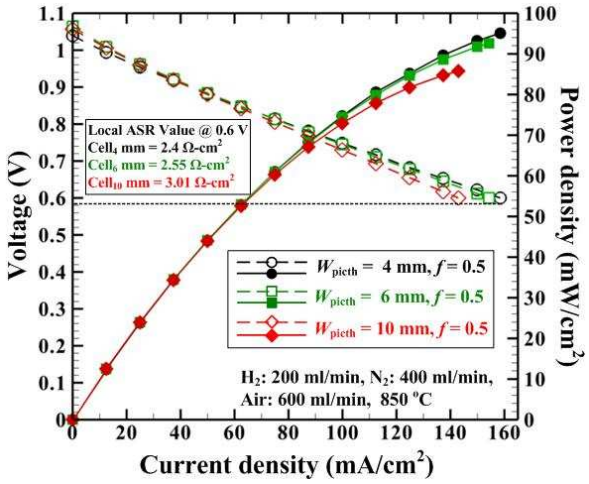

圖 3.2 不同 W_{pitch} 對電池性能的影響。

電化學阻抗頻譜量測結果如圖 3.3 所示，可發現當 W_{pitch} 值越小時，其阻抗頻譜曲線越小，但是歐姆阻抗則幾乎相同。這是由於 f 值固定時，W_{pitch} 值越大則 W_{pin} 值越大，故造成氣體越難擴散至 pin 下方進行電化學反應，因此造成濃度損失增加。另一方面，三種 W_{pitch} 尺寸設計中雙極板與電極的有效接觸面積皆相近，因此接觸電阻相近，歐姆阻抗亦幾乎相同，此實驗結果與 Gazzarri & Kesler [27]之數值模擬結果相同。而由於歐姆阻抗幾乎相同，故可推斷 W_{pitch} 效應中，電流傳遞路徑所主導之傳遞電阻，對於電池性能之影響是微乎其微。

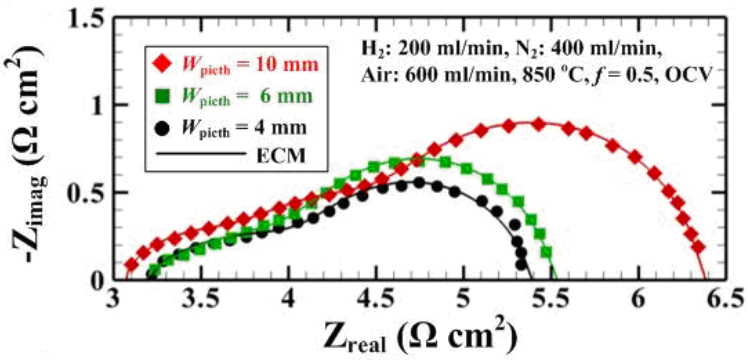

圖 3.3 不同 W_{pitch} 在 OCV 條件下對阻抗頻譜的影響。

在此固定 W_{pitch} 值為 4 mm，探討 f 值分別為 0.33、0.5，以及 0.66 時，電池性能的差異，此三種尺寸設計的 W_{pin} 分別為 1.32 mm、2 mm，以及 2.64 mm，而 pin 與電極的有效接觸面積比則分別為 11 %、24 %，以及 45%。

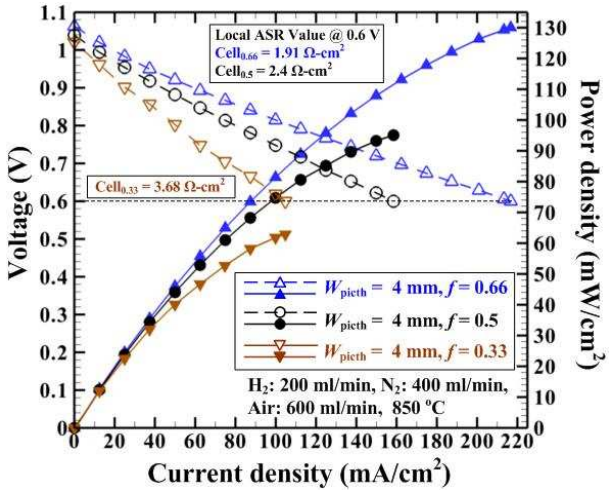

圖 3.4 不同 f 值對電池性能的影響。

電化學阻抗頻譜量測結果如圖 3.5 所示，可發現當 f 值變化時，其阻抗頻譜曲線大小相當，但是歐姆阻抗卻隨 f 值減少而增加。這

是由於 W_{pitch} 值固定時，f 值越小則 pin 與電極之間的有效接觸面積越小，因此造成較大的接觸電阻，故導致歐姆損失增加。另一方面，f 值越小則 W_{pin} 值越小，雖然濃度損失會降少，然而此減少量卻遠不及歐姆損失的增加量，因此整體電池性能隨 f 值減少而降低。

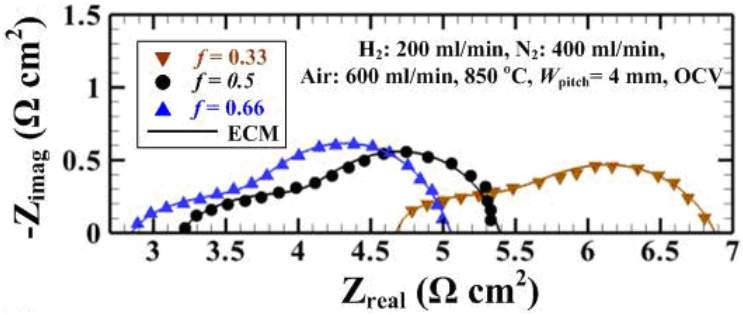

圖 3.5 不同 f 值在 OCV 條件下對阻抗頻譜的影響

等效電路模組分析，阻抗區分為歐姆阻抗(R_Ω)與極化阻抗(R_P)，本實驗 R_Ω 值顯而易見，可由阻抗曲線高頻區與阻抗實軸交界處所獲得，然而阻抗曲線低頻區卻沒有與阻抗實軸相交，因此必須藉由等效電路模組分析，近一步得知本實驗的 R_P。本實驗所建立的等效電路模組及阻抗數學式如圖 3.6 (a)所示，其等效電路元件包括一個電阻(R_Ω)、一個電桿(L)，以及三組電阻(R)與恆相位元素(P)並聯之組件(簡稱為 RP 元件)，而如 3.3 圖及圖 3.5 所示，數學式所呈現的 ECM 曲線可與實驗數據契合，故以此數學式為基礎，降低角頻率(ω)使其模擬曲線與阻抗實軸相交，如此便可得知本實驗的 R_P，其示意圖如圖 3.6 (b)。

(a)

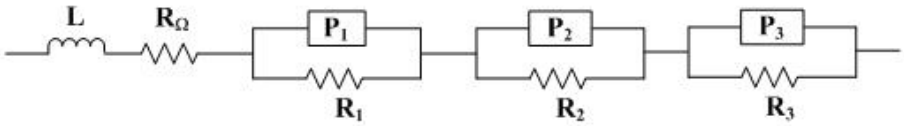

$$Z(\omega) = L(i\omega) + R_\Omega + \frac{R_1}{R_1Q_1(i\omega)^{n_1}+1} + \frac{R_2}{R_2Q_2(i\omega)^{n_2}+1} + \frac{R_3}{R_3Q_3(i\omega)^{n_3}+1}$$

(b)

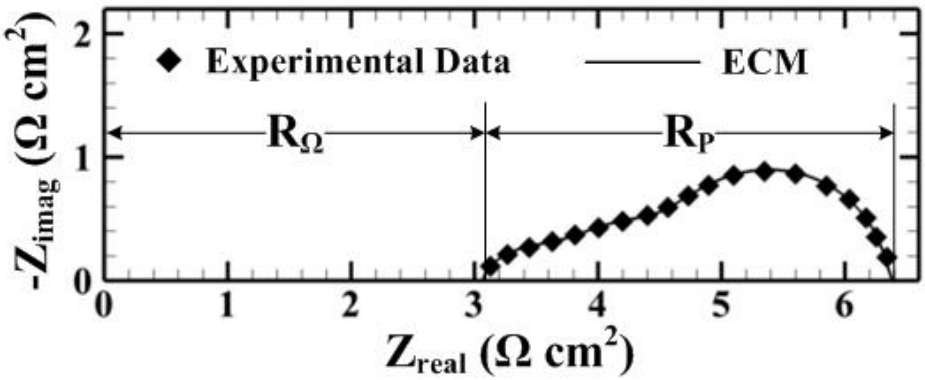

圖 3.6 (a)本實驗所建立的等效電路模組；(b)本實驗的歐姆阻抗(R_Ω)與極化阻抗(R_P)示意圖，以及等效電路模組曲線(實線)與實驗數據契合情況(以 W_{pitch} = 10 mm、f = 0.5，OCV 條件為例)。

圖 3.7 顯示不同流道尺寸設計的阻抗比較，由圖 3.7 (a)可發現，W_{pitch} 值效應造成電池性能差異的原因，主要來自 R_P 的變化，R_P 隨 W_{pitch} 值減少而明顯減少，這由於較小的 W_{pitch} 值，則 W_{pin} 值較小，反應氣體較易擴散至 pin 下方的電極進行反應，濃度損失較小，因此 R_P 較小。此外，雖然 R_Ω 隨 W_{pitch} 值減少而稍微增加，但與 R_P 變化的幅度相比，R_Ω 變化幾乎可以忽略，這是由於 f 值固定，則雙極板與電極間有效接觸面積相近，接觸電阻相近，因此 R_Ω 皆相近。另

一方面，由圖 3.7 (b)可發現，f 值效應造成電池性能差異的原因，主要來自 R_Ω 的變化，較大的 f 值，其 R_Ω 較小，而 R_P 卻幾乎相同。這是由於較大的 f 值，則雙極板與電極間有效接觸面積較大，接觸電阻較小，因此 R_Ω 越小。而 R_P 相近的原因，估計是因為反應氣體於 pin 下方的擴散距離，已大於 pin 的寬度，因此濃度損失相近[28]。此外，由本實驗可發現，f 值固定為 0.5，W_{pitch} 分別為 4 mm、6 mm 時，以及 W_{pitch} 固定為 4 mm，f 值分別為 0.33、0.5、0.66 時，其 R_P 皆沒有明顯差異，顯示當 W_{pin} 小於 3 mm 時，即可避免濃度損失的增加。

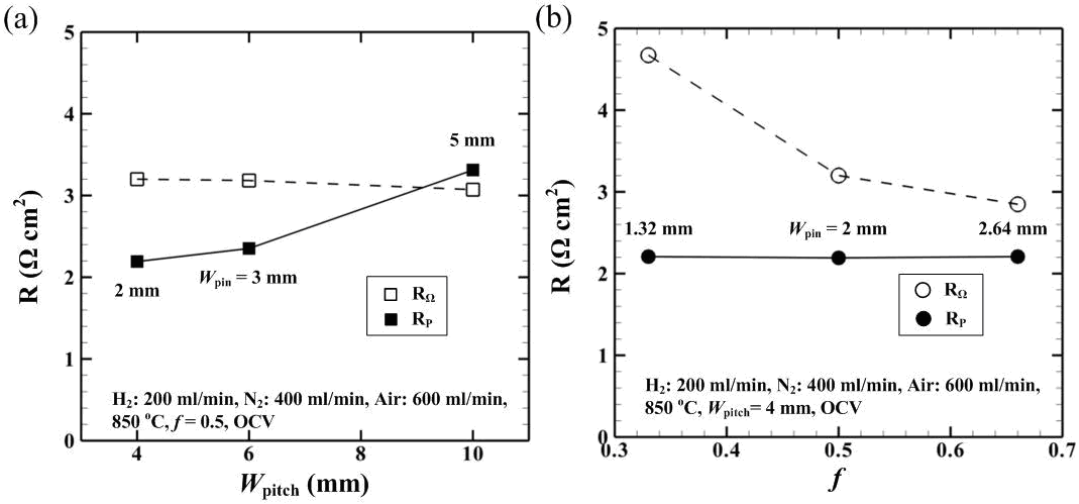

圖 3.7 不同流道尺寸設計的阻抗比較：(a)不同 W_{pitch}；(b)不同 f 值。

圖 3.8 顯示不同流道尺寸設計於不同操作電壓下，R_Ω 與 R_P 的比較。可發現當操作電壓減少時， R_P 將減少，而 R_Ω 則幾乎不會變化。這是由於降低操作電壓，會使得電化學反應更加劇烈，因此增加電

極活性。故 R_P 減少，而 R_Ω 與電化學反應無關，因此不會有明顯變化。而此可知，考量真實電池操作條件，如何降低電池堆 R_Ω 顯的更加得重要。

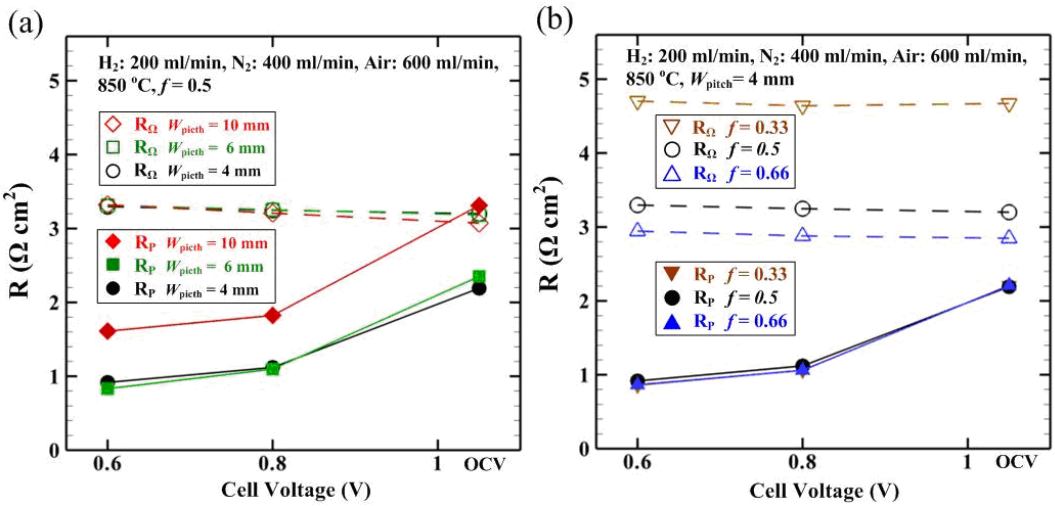

圖 3.8 不同流道尺寸設計於不同操作電壓下的阻抗比較：(a) 不同 W_{pitch}；(b) 不同 f 值。

由本實驗結果可知，f 值效應影響 R_Ω 變化，進而造成電池性能差異，很明顯地，影響 R_Ω 的主要物理化學機制，是雙極板與電極間有效接觸面積所主導的接觸電阻。然而，W_{pitch} 效應所影響的主要物理化學機制卻無法如上述般直接判斷，這是由於 R_P 包括電極電化學反應阻抗及反應氣體擴散阻抗，因此無法直接認定是何種物理化學機制造成 R_P 的變化。

數值模擬研究可直接由阻抗頻譜中阻抗峰值所獲得 f_{summit}，進而得知影響電池性能的各種物理化學反應機制。然而，真實實驗的電

化學反應較數值模擬所假設的複雜許多，阻抗頻譜中阻抗峰值並不明顯，因此無法直接獲得各個阻抗之 f_{summit}。對於這種情況，f_{summit} 需透過下列方程式[29]，藉由 ECM 數據計算獲得：

$$f_{summit} = \frac{1}{2\pi}(RC)^{-\frac{1}{n}} \quad (4.1)$$

其中 R 為電阻；C 為電容(n = 1 時，P = C)；n 為恆相位元素中的指數。藉由此方法，便可得知 ECM 各組件的 f_{summit}，進而了解各組件所代表的物理化學反應機制。W_{pitch} 效應的 ECM 數據如表 1 所示。比對三組 RP 元件的 f_{summit}，結果顯示 R_1P_1 元件($f_{summit,1}$ = 0.4 ~ 0.6)代表陰極電化學反應阻抗(f_{summit} ~ 0.5)[30]；R_2P_2 元件($f_{summit,2}$ = 0.4 ~ 0.6)代表反應氣體擴散阻抗(f_{summit} = 10 ~ 100 Hz)[31]；R_3P_3 元件($f_{summit,3}$ ~ 400 Hz)代表陽極電化學反應阻抗(f_{summit} > 100 Hz)[32]。由數據中可發現反應氣體擴散阻抗中，Q_2 隨 W_{pitch} 增加而減少，這顯示 W_{pitch} 效應將影響電池反應氣體擴散阻抗，且阻抗隨 W_{pitch} 值增加而增加(Q_2 與 Z_P 為倒數關係，$Z_P = Q^{-1}(j\omega)^{-n}$)。此外，$W_{pitch}$ 值增加亦導致陰極電化學反應阻抗與陽極電化學反應阻抗增加，且陰極電化學反應阻抗增加情況較陽極嚴重。由此可知，W_{pitch} 效應確實將影響反應氣體擴散情況，且較大的 W_{pitch}，其濃度損失越嚴重，此實驗結果與 Gazzarri & Kesler[27]數值結果類似，並可驗證所有數值團隊對於濃度損失增加的解釋。

表 1 不同 W_{pitch} 之等效電路模組數據比較(f 值皆為 0.5)。

W_{pitch} (mm)	4	6	10
L (μH)	0.141	0.144	0.136
R_{Ω} (Ω)	0.200	0.199	0.192
Q_1 (F)	4.345	4.331	3.631
n_1	1.000	0.942	1.000
R_1 (Ω)	0.057	0.085	0.091
Q_2 (F)	1.288	1.191	0.880
n_2	0.632	0.664	0.609
R_2 (Ω)	0.056	0.046	0.094
Q_3 (F)	0.072	0.057	0.033
n_3	0.813	0.911	0.921
R_3 (Ω)	0.022	0.013	0.021
$f_{summit,1}$ (Hz)	0.644	0.459	0.480
$f_{summit,2}$ (Hz)	10.086	12.528	9.560
$f_{summit,3}$ (Hz)	450.717	429.309	437.389

二、結論與建議

綜合本研究所獲得的各項數據，包含實驗量測與數值模擬，我們歸納出下列幾點結論、具體成果與建議：

(1) 本團隊利用計畫所建立的單電池堆性能測試平台與標準實驗流程，進行改善並用至加壓型單電池堆性能測試平台。目前加壓型單電池堆設備已建立完成，並進行實驗流測試。未來將進行發電測試，並利用電化學阻抗頻譜量測，探討壓力效應對電池性能之影響。

(2) 本團隊在一系列的棋盤式雙極板尺寸效應實驗裡，我們找到優化流道尺寸為 W_{pitch} = 4 mm 和 f = 0.66。此研究結果應有助於提升棋盤式 SOFC 電池性能及壽命。

(3) 新式壓縮密封材料陶瓷纖維紙的實驗裡我們找出優化製備程序，未來將進行在高壓環境下測試。

(4) 已與李堅雄博士共同發表兩篇 SCI 論文於 Journal of Power Sources，內容請參見附件二與附件三。

(5) 與投稿兩篇會議論文至亞洲 SOFC 會議。題目分別為：(1) The impact of flow distributors on the performance of solid oxide fuel cell: power generating characteristics and electrochemical impedance measurements；(2) Planar solid oxide fuel cells: cell performance and impedance measurements of single-cell stacks using pin-type flow channels with various sizes。已被接受發表，此會議已於今年 9 月 5 日 ~ 7 日在日本京都舉行。計畫主持人和其碩士生張軒維同學一齊前往日本京都並發表論文。

(6) 投稿一篇會議論文至中國機械工程師學會第 27 屆全國學術研討

會，題目為“棋盤式雙極板尺寸效應對固態氧化物燃料電池性能之影響”，此會議已於今年 12 月 10 ~ 11 日在台北科技大學舉辦，已由計畫主持人碩二學生張軒維先生前往報告。

(7) 投稿一篇會議論文至中華民國力學學會年會暨第 34 屆全國力學研討會，題目為“實驗量測分析 Kee’s 燃料電池堆流場分佈模式之可靠度”，此會議於今年 11 月 19 ~20 日在雲林科技大學舉辦。將由計畫主持人碩一學生鄭浩昇先生前往報告。

參考文獻

[1] Stambouli, A.B. and Traversa, E., Solid oxide fuel cells (SOFCs): a review of an environmentally clean and efficient source of energy, *Renew. Sust. Energ. Rev.* Vol. **6**, pp. 433-455, 2002.

[2] Williams, M.C., Strakey, J.P. and Surdoval, W.A., The U.S. department of energy, office of fossil energy stationary fuel cell program, *J. Power Sources*, Vol. **43**, pp. 191-196, 2005.

[3] Lee, C.H., Lee, M.C., Hwang, C.S., Lee, R.Y. and Lin, L.F., SOFC development at INER, *Int. J. Appl. Ceram. Technol.*, Vol. **4**, pp. 339-349, 2007.

[4] Liu, H.C., Lee, C.H., Shiu, Y.H., Lee, R.Y. and Yan, W.M., Performance simulation for an anode-supported SOFC using Star-CD code, *J. Power Sources*, Vol. **167**, pp. 406-412, 2007.

[5] Chiang, L.K., Liu, H.C., Shiu, Y.H., Lee, C.H. and Lee, R.Y., Thermal stress and thermo-electrochemical analysis of a planar anode-supported solid oxide fuel cell: Effects of anode porosity, *J. Power Sources*, Vol. **195**, pp. 1895-1904, 2010.

[6] Yen, T.H., Hong, W.T., Huang, W.P., Tsai, T.C., Wang, H.Y., Huang, C.N. and Lee, C.H., Experimental investigation of 1 kW solid oxide fuel cell system with a natural gas reformer and an exhaust gas burner, *J. Power Sources*, Vol. **195**, pp. 1454-1462, 2010.

[7] Veyo, S.E., Shockling, L.A., Dederer, J.T., Gillett, J.E. and Lundberg, W.L., Tubular solid oxide fuel cell/gas turbine hybrid cycle power systems: status, *J. Eng. Gas. Turbines Power-Trans. ASME*, Vol. **124**, pp.845-849, 2002.

[8] Yang, W.J., Park, S.K., Kim, T.S., Kim, J.H., Sohn, J.L. and Ro, S.T., Design performance analysis of pressurized solid oxide fuel cell/gas turbine hybrid systems considering temperature constraints, *J. Power Sources*, Vol. **160**, pp. 462-472, 2006.

[9] Huang, C.M., Shy, S.S. and Lee, C.H., On flow uniformity in various interconnects and its influence to cell performance of planar SOFC, *J. Power Sources*, Vol. **183**, pp. 205-213, 2008.

[10] Huang, C.M. Shy, S.S., Huang, S.C. and Lee, C.H., Performance measurements of a single-cell stack using various designs of flow distributors for planar SOFC, *ECS Transactions*, Vol. **25**, No. 2, pp.

221-230, 2009.

[11] Singhal, S.C. and Kendall, K., *High temperature solid oxide fuel cells: fundamentals, design and applications*, Elsevier Ltd., Kidlington, UK, 2003.

[12] Larminie, J. and Dicks, A., *Fuel cell systems explained*, 2nd Eds., John Wiley & Sons Ltd., West Sussex, England, 2003.

[13] Veyo, S. E., Shockling, L. A., Dederer, J. T., Gillett, J. E., Lundberg, W. L., Tubular Solid Oxide Fuel Cell/Gas Turbine Hybrid Cycle Power Systems: Status, *Journal of Engineering for Gas Turbines and Power,* Vol. **124**, pp. 845-849, 2002

[14] Yi, Y., Rao, A.D., Brouwer, J. and Samuelsen, G.S., Analysis and optimization of a solid oxide fuel cell and intercooled gas turbine (SOFC-ICGT) hybrid cycle, *J. Power Sources*, Vol. **132**, pp. 77-85, 2004.

[15] Park, S.K. and Kim, T.S., Comparison between pressurized design and ambient pressure design of hybrid solid oxide fuel cell-gas turbine systems, *J. Power Sources*, Vol. **163**, pp. 490-499, 2006.

[16] Arsalis, A., Thermoeconomic modeling and parametric study of hybrid SOFC–gas turbine–steam turbine power plants ranging from 1.5 to 10 MWe, *J. Power Sources*, Vol. **181**, pp. 313-326, 2008.

[17] Ni, M., Leung, M.K.H. and Leung, D.Y.C., Parametric study of solid oxide fuel cell performance, *Energy Conv. Manag*., Vol. **48**, pp. 1525–1535, 2007.

[18] Patcharavorachot, Y., Arpornwichanop, A. and Chuachuensuk, A., Electrochemical study of a planar solid oxide fuel cell: role of support structures, *J. Power Sources*, Vol. **177**, pp. 254-261, 2008.

[19] Bo, C., Yuan, C., Zhao, X., Wu, C.B. and Li, M.Q., Parametric analysis of solid oxide fuel cell, *Clean Techn. Environ. Policy*, Vol. **11**, pp. 391-399, 2009.

[20] Honeywell, *Solid oxide fuel cell hybrid system for distributed power generation*, Quarterly Technical Progress Report, DE-FC26-01NT40779, 2002.

[21] Zhou, L., Chen, M., Yi, B., Dong, Y., Cong, Y. and Yang, W., Performance of an anode-supported tubular solid oxide fuel cell

(SOFC) under pressurized conditions, *Electrochim. Acta*, Vol. **53**, pp. 5195-5198, 2008.

[22] Thomsen, E.C., Coffey, G.W., Pederson, L.R. and Marina, O.A., Performance of lanthanum strontium manganite electrodes at high pressure, *J. Power Sources*, Vol. **191**, pp. 217–224, 2009.

[23] Lim, T.H., Song, R.H., Shin, D.R., Yang, J.I., Jung, H., Vinke, I.C. and Yang, S.S., Operating characteristics of a 5 kW class anode-supported planar SOFC stack for a fuel cell/gas turbine hybrid system, *Int. J. Hydro. Energy*, Vol. **33**, pp. 1076-1083, 2008.

[24] Huang, C.M., Shy, S.S. and Lee, C.H., The impact of flow distributors on the performance of planar solid oxide fuel cell, *J. Power Sources*, Vol. **195**, pp. 6280-6286, 2010

[25]Chou, Y.S., Stevenson, J.W., Chick, L.A., Ultra-low leak rate of hybrid compressive mica seals for solid oxide fuel cells, *J. Power Sources*, Vol. **112**, pp. 130-136, 2002

[26] 李信宏，2010，棋盤式雙極板尺寸效應對固態氧化物燃料電池性能之影響，*碩士論文*，國立中央大學機械系。

[27] Gazzarri, J.I. and Kesler, O., Short-stack modeling of degradation in solid oxide fuel cells: Part I. Contact degradation, *J. Power Sources*, Vol. **176**, pp. 138-154, 2008.

[28] Lin, Z., Stevenson, J. W. and Khaleel, M. A., The effect of interconnect rib size on the fuel cell concentration polarization in planar SOFCs, *J. Power Sources*, Vol. **117**, pp. 92-97, 2003.

[29] Barfod, R., Mogensen, M., Klemensø, T., Hagen, A., Liu, Y.L. and Hendriksen, P.V., Detialed characterization of anode-supported SOFCs by impedance spectroscopy, *J. Electrochem. Soc.*, Vol. **154**, pp. B371-B378, 2007.

[30] Jørgensenz, M. J. and Mogensen, M., Impedance of solid oxide fuel cell LSM/YSZ composite cathodes, *J. Electrochem. Soc.*, Vol. **148**, Issue 5, pp. A433-A442, 2001.

[31] Primdahl, S. and Mogensen, M., Gas diffusion impedance in characterization of solid oxide fuel cell anodes, *J. Electrochem. Soc.*, Vol. **146**, Issue 8, pp. 2827-2833, 1999.

[32] Primdahl, S. and Mogensen, M., Gas conversion impedance: A test

geometry effect in characterization of solid oxide fuel cell anodes, *J. Electrochem. Soc.*, Vol. **145**, Issue 7, pp. 2431-2437, 1998.

附件一、等效電路模組(ECM)數據分析流程。

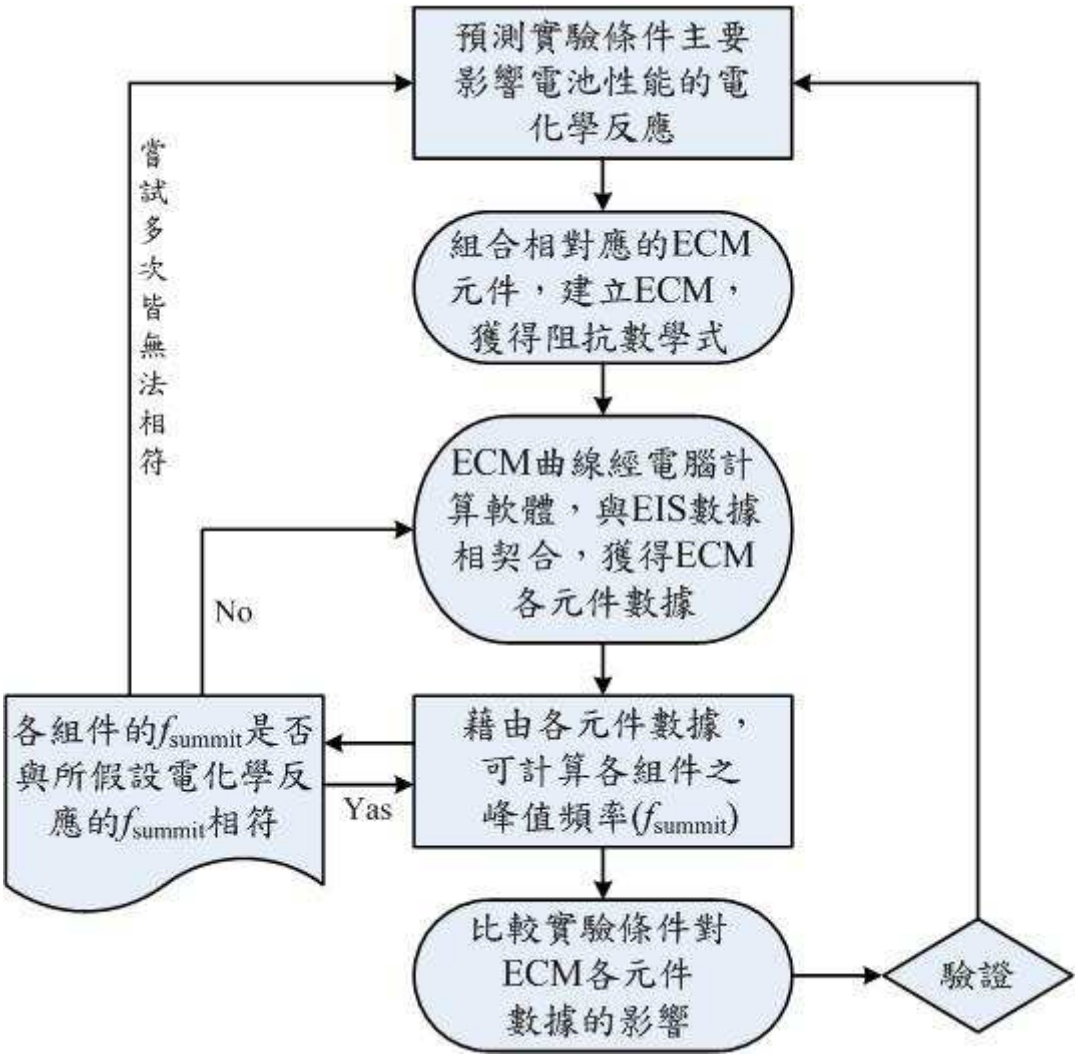

附件二、本年度發表於 Journal of Power Sources 的論文(SCI)

Journal of Power Sources 195 (2010) 2260–2265

Contents lists available at ScienceDirect

Journal of Power Sources

journal homepage: www.elsevier.com/locate/jpowsour

Parametric study of anodic microstructures to cell performance of planar solid oxide fuel cell using measured porous transport properties

C.M. Huang[a], S.S. Shy[a,*], C.W. Chien[a], C.H. Lee[b]

[a] Department of Mechanical Engineering, National Central University, 300 Jhong-da Road, Jhong-li 32001, Taiwan
[b] Institute of Nuclear Energy Research, Lung-tan, Tao-yuan 32546, Taiwan

ARTICLE INFO

Article history:
Received 8 September 2009
Received in revised form 14 October 2009
Accepted 15 October 2009
Available online 24 October 2009

Keywords:
Anodic microstructures
Porosity
Permeability and tortuosity
Peak power density
Porous slip velocity
Brinkman equation

ABSTRACT

This study reports effects of porosity (ε), permeability (k) and tortuosity (τ) of anodic microstructures to peak power density (PPD) of a single-unit planar anode-supported SOFC based on 3D electrochemical flow models using measured porous transport properties. Applying particle image velocimetry, a transparent porous rib-channel with different ε is applied to measure an effective viscosity (μ_e) in the Brinkman equation commonly used to predict flow properties in porous electrodes. It is found that, contrary to the popular scenario, μ_e is not equal to the fluid viscosity (μ_f), but it is several orders in magnitude smaller than μ_f resulting in more than 10% difference on values of PPD. Numerical analyses show: (1) while keeping k and τ fixed with ε varying from 0.2 to 0.6, the highest PPD occurs at $\varepsilon = 0.3$ where the corresponding triple-phase-boundary length is a maximum; (2) PPD increases slightly with k when $k \leq 10^{-11}$ m^2 due to the diffusion limitation in anode; and (3) PPD decreases with τ when $\tau > 1.5$ due to the accumulation of non-depleted products. Hence, a combination of $\varepsilon = 0.3$, $k = 10^{-11}$ m^2, and $\tau = 1.5$ is suggested for achieving higher cell performance of planar SOFC.

1. Introduction

There is great interest in using the anode-supported solid oxide fuel cell (SOFC), because its thin electrolyte may signify it can generate electricity at reduced temperature ranging from 600 °C to 800 °C. In this temperature range, various low-cost materials can be applied to the cell and its auxiliary components, and as such, the influences of thermal cycles and thermal stresses to the cell's longevity may be mitigated [1]. On the other hand, when thick anodic electrodes are used, it is difficult to supply enough fuel to the reaction site commonly known as the triple-phase-boundary (TPB) [2]. Clearly, there is a need to carefully deal with the cell concentration polarization problem by the investigation of effects of anodic microstructure properties including such as porosity (ε), permeability (k) and tortuosity (τ) to cell performance, so that the anode-supported SOFC can be operated more properly at reduced temperatures. This motivates the present work.

Recently, many geometrical and numerical models have been developed to predict optimal electrodes' microstructures in attempt to enhance the cell performance of SOFCs. For instances, Deng and Petric [3] proposed a geometrical model to maximize the TPB length of the electrodes when both pore and grain sizes of 1 μm with $\varepsilon = 0.3$ were used. Ni et al. [4] developed an electrochemical model based on the Bulter–Volmer equation, Fick's law and Ohm's law to study the influence of electrodes' microstructures to the cell performance. They found that the cell power can be maximized when the electrodes with a pore size of 3 μm and $\varepsilon = 0.4$ were used. Various numerical models were also developed to investigate the effect of the electrode's thickness to the cell performance of anode-supported SOFCs [5–7]. Though considerable progress has been made in understanding the influence of anodic microstructures to cell performance of planar SOFC, the actual transport phenomena occurring between flow distributors and porous electrodes which are crucial to the concentration polarization still remain unclear.

For planar anode-supported SOFCs, the momentum transfer in porous rib-channels of flow distributors features the supply of fuel and oxidant to the electrodes and thus has great influence on heat and species transports. In order to predict correctly the cell performance, proper flow models with accurate boundary conditions at the porous interface of rib-channels are required. Fig. 1 shows a typical variation of velocity profiles in a rib-channel across the anode. In it there are three different flow regions: (1) a free flow region with a nearly parabolic velocity profile which is governed by the second-order Navier–Stokes (N–S) equations, (2) a transitional region where the flow velocity decreases drastically until it reaches the Darcy's velocity, and (3) a porous region where the flow velocity is almost constant and is governed by the first-order Darcy's law [8]. Obviously, flow velocities and shear stresses in the transitional region cannot be matched by the second-order N–S equations

* Corresponding author. Tel.: +886 3 426 7327; fax: +886 3 427 6157.
E-mail address: sshy@ncu.edu.tw (S.S. Shy).

0378-7753/$ – see front matter © 2009 Elsevier B.V. All rights reserved.
doi:10.1016/j.jpowsour.2009.10.048

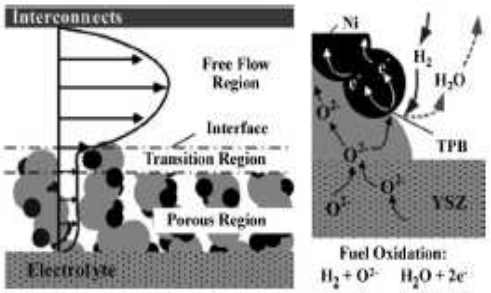

Fig. 1. Left: schematic velocity profiles across an anodic porous rib-channel between interconnect and electrolyte of a planar SOFC including three different flow regions. Right: a cartoon showing the fuel oxidation process occurred around the triple-phase-boundary (TPB).

and the first-order Darcy's law. Therefore, various approaches have been taken into consideration to solve such matching problem in numerical simulations, of which we introduce two most commonly used equations. The first equation was proposed by Brinkman [9] in a form of

$$\nabla p = -\left(\frac{\mu_f}{k}\right) U + \mu_e \nabla^2 U, \tag{1}$$

where p, μ_f, μ_e, k, and U were the pressure, the fluid dynamic viscosity, the effective viscosity, the permeability, and the flow velocity. Eq. (1) is an extension of the Darcy's law with an additional second-order body force term ($\mu_e \nabla^2 U$), where μ_e acts as a fitting parameter. The second equation proposed by Beavers and Joseph [10] (hereafter refer to B&J) was a semi-empirical slip boundary condition at the porous interface indicating the strain rate just on the top of the porous interface,

$$\frac{du}{dy}\Big|_{y=0^+} = \frac{\alpha}{\sqrt{k}}(U_s - U_D), \tag{2}$$

where U_s is the free fluid velocity at the interface (the slip velocity), U_D is the Darcy's velocity, α is a slip coefficient, and k is the permeability of the porous medium. Since U_D is much smaller than U_s, Eq. (2) may be simplified to

$$\alpha = \dot{\gamma}\frac{\sqrt{k}}{U_s}, \tag{3}$$

where $\dot{\gamma} = du/dy|_{y=0^+}$. It should be noted that the slip velocities obtained from the Brinkman equation and the B&J boundary condition are equivalent when $\alpha = (\mu_e/\mu_f)^{0.5}$, as confirmed by Neal and Nader [11]. Values of α may vary from 0.1 to 4 depending on the properties of porous media [10]. Moreover, an important experimental finding by Givler and Altobellic [12] showed that μ_e can be equal to μ_f ($\alpha = 1$) only when $\varepsilon > 0.9$ in porous flows. Without the consideration of this experimental evidence, all current available numerical studies in modeling the momentum transport for SOFCs, see Refs. [13–16] among many others, all assumed $\mu_e = \mu_f$ in the Brinkman equation even though values of ε for SOFCs are within $0.2 < \varepsilon < 0.4$ which are much smaller than 0.9. To validate such assumption ($\mu_e = \mu_f$) used in the Brinkman equation, this study introduces an experimental platform for quantitative measurements of slip velocities at the porous interface with porosity closely matching that of SOFCs. Hence, the information on μ_e in the Brinkman equation (Eq. (1)) or α (Eq. (3)) may be obtained and the complex momentum transport across the porous interface of SOFCs may be investigated.

Table 1
Material properties of various porous media used in this study.

Porous media	ε	$k^{0.5}$ (mm)	τ
Al_2O_3	0.04	1.1×10^{-4}	1.85
ZrO_2	0.17	3.87×10^{-4}	1.73
Ni-mesh	0.43	2.74×10^{-3}	1.48

As the first objective, we measure slip velocities very near the porous interface using a prototypical porous rib-channel with values of ε ranging from 0 to 0.43 in a gaseous experimental platform using particle image velocimetry (PIV) and thus values of μ_e may be obtained. The second but equally important objective is to perform numerical sensitivity tests on effects of anodic microstructures to the cell performance. As shown on the right of Fig. 1, the main role of an anode is to provide the active sites for the electrochemical reaction, so that the oxide ions (O^{2-}) available from the electrolyte can react with the fuel at the TPB which locates around the contorted boundaries among the electrolyte, the electro-catalyst, and the gaseous fuel. This is why anodic microstructures are so crucial to the concentration polarization of the anode-supported SOFCs. As noted previously, quite a few studies are available for effects of anodic pore and grain sizes to the cell performance (e.g., Refs. [3–7]). However, very few studies are available for effects of k and τ to the cell performance. As pointed out by Koponen et al. [17], k represents the ability of the porous media to transmit fluid and τ indicates the shortest continuous flow paths between any two points within the pore space. An anode with proper values of k and τ can significantly improve the pathway of the gases within the porous electrodes which in turn can further increase the cell performance. Therefore, this study investigates numerically effects of ε, k, and τ to the cell performance of a single-unit planar anode-supported SOFC.

The following sections describe experimental methods used in this study, concerning measurements of gaseous velocity fields in porous rib-channels using PIV. A 3D electrochemical flow model for a single-unit planar anode-supported SOFC is then presented. Using the measured boundary conditions at the porous interface,

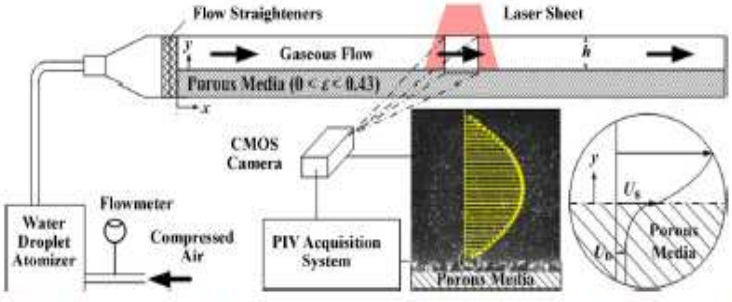

Fig. 2. The gaseous experimental platform for velocity measurements in a porous rib-channel using PIV, where U_s is the slip velocity at the porous interface and U_D is the Darcy velocity.

numerical simulations are performed and effects of various anodic microstructures to cell performance of the single-unit cell stack are discussed. Finally, conclusions are offered.

2. Experimental methods

Fig. 2 presents a gaseous platform consisting of a Plexiglas rib-channel with different porous materials, a TSI atomizer for seeding particles, and a PIV acquisition system. Three different porous media with different values of ε are applied, respectively, $\varepsilon = 0.04$ for aluminum oxide (Al_2O_3), $\varepsilon = 0.17$ for chromium oxide (ZrO_2), and $\varepsilon = 0.43$ for nickel mesh (Ni-mesh), which have microstructures similar to commonly used anodic materials for planar anode-supported SOFCs. These porous media are placed on the bottom of the rib-channel, so that velocity distributions in the porous rib-channel can be measured by PIV. In this study, a mercury intrusion porosimeter (Porous Materials, Inc., USA), is used to measure the porous properties (ε, k, and τ) of these three porous media, as listed in Table 1. The working fluid is air and its flow rate is controlled by a flowmeter mounted between the air bottle and the atomizer. A hydraulic Reynolds number ($Re = UD_h/\nu$) based on the hydraulic diameter of the rib-channel above the porous media is used to characterize the flow, where U is the mean velocity and ν is the kinematic viscosity of the working fluid. For simplicity, the present work considers a flow with fixed $Re = 100$ and measures corresponding velocity profiles in these porous rib-channels having different values of ε.

As can be also seen from Fig. 2, the coordinates, x and y, denote streamwise and transverse directions, with $x = 0$ at the inlet of the rib-channel and $y = 0$ at the porous interface. In order to perform PIV measurements, a small amount of tiny water droplets with a mean diameter of 3 μm issuing from the TSI atomizer was provided to the air flow. We applied 10 W diode laser with appropriate optical lenses to generate a laser sheet that cut the seeding flow in the middle of the rib-channel (see Fig. 2). A high-speed CMOS camera (512 × 512 pixels) positioned perpendicular to the plane of the laser sheet was used to record the evolution of the flow through the porous rib-channel using a frame rate of 2000 frames s^{-1} with a view field of 8.1 mm × 8.1 mm. All acquired images were then post-processed by a Matlab-based cross-correlation software using an interrogation window of 32 × 32 pixels with 75% overlapping. For detail treatment of PIV measurements, the reader is directed to Ref. [18]. An ensemble-average velocity profile in the porous rib-channel superimposed on an instantaneous flow image is also presented in Fig. 2, where the porous medium used is Ni-mesh. Due to the optical limitation, we cannot measure the velocity profiles inside the porous media using the current gaseous platform.

3. Numerical simulation

Fig. 3a shows a single planar SOFC stack consisting of a positive-electrode/electrolyte/negative-electrode (PEN) and a pair of interconnects with rib-channels to distribute fuel and air through the PEN. In order to correctly simulate various transport phenomena and electrochemical reactions occurring near the porous interface and the PEN, sufficiently dense computational grids must be applied to these regions. For simplicity, a 3D reacting model with one unit of the single-cell stack, as shown in Fig. 3b is considered, where the co-flow arrangement is applied for both anode and cathode, having a total grid-number of 250,000 for simulation (already very time-consuming). Using this 3D single-unit cell stack model, sensitive tests on effects of ε, k and τ to cell performance are performed, in which only one variable is changed at a time with the other variables fixed. The conservation equations of mass, momentum, energy, and species together with the fuel-reforming reactions and electrochemical reactions in the planar single-unit cell stack are solved using the CFD-RC package based on a finite volume approach with appropriate computational grids.

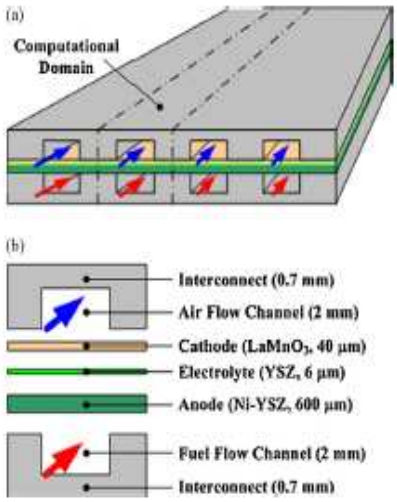

Fig. 3. (a) Schematic of a single anode-supported planar SOFC using the co-flow arrangement. (b) Same as (a), but for a single-unit cell used in a 3D reacting flow model.

Since the simulations for both non-reacting and reacting flows are performed in a steady state condition, the mass continuity equation can be described by

$$\nabla \cdot (\varepsilon \rho \vec{U}) = S_m, \tag{4}$$

where ε is the porosity, ρ is the density of the multi-component gas mixture calculated by the ideal gas law, and S_m is a source term generated by chemical and electrochemical reactions. The laminar incompressible momentum equation can be written in a form of

$$\nabla \cdot (\varepsilon \rho \vec{U}\vec{U}) = -\varepsilon \nabla p - \frac{\varepsilon^2 \mu_f \vec{U}}{k} + \varepsilon \mu_e \nabla^2 \vec{U}, \tag{5}$$

where p is the pressure. The energy equation is

$$\nabla \cdot (\varepsilon \rho \vec{U} h_0) = \nabla \cdot \vec{q} + \varepsilon \vec{\delta} \nabla \vec{U} + S_e \tag{6}$$

where h_0 is the enthalpy of the gases, $\vec{q}$ is the heat flux, and S_e is the heat source term from the heat transport and the species diffusion. The variations of thermal properties for both gases and solid materials with temperature are also considered in the simulation. The species conservation equation can be expressed

$$\nabla \cdot (\varepsilon \rho Y_i) = \nabla \cdot J_i + \omega_i, \tag{7}$$

where Y_i, J_i, and w_i are the mass fraction, the diffusion flux, and the production rate of the ith species in the gas phase, respectively. In this study, the transport properties, such as the species diffusivities are calculated using a sub-model based on the Stefan–Maxwell equation. Finally, a Bulter–Volmer equation is applied for the correlation between electrochemical reactions and current density in the catalytic layer, as shown below

$$j = j_0 \left[\exp\left(\frac{\lambda_a F}{RT}\right)\eta - \exp\left(\frac{\lambda_c F}{RT}\right)\eta \right] \prod_{i=1}^{N} [i]^{\beta_i}, \tag{8}$$

where λ_a and λ_c are the kinetic constants determined from the experimental Tafel slopes [19], j and j_0 are the current density and the reference current density at a known open circuit voltage, and F and R are the Faraday constant and the gas constant, respectively. The other parameters in Eq. (8) are the overpotential between the electronic and ionic phases (η), the interfacial concentration of ith species ($[i]$), the total number of reacting species (N), and the concentration exponents of the ith species (β_i), respectively.

In this study, fuels are syn-gases with 9.6% H_2, 26% CO, 21.6% CO_2, and 42.8% H_2O based on the mass fraction. The composition of air is 79% N_2 and 21% O_2. For the anode, hydrogen is oxidized via $H_2 + O^{2-} \rightarrow H_2O + 2e^-$. Simultaneously, the reduction of oxidant occurs at the cathode is via $0.5\ O_2 + 2e^- \rightarrow O^{2-}$. Since hydrogen can be reformed from carbon monoxide at high-temperature conditions, the water–gas-shift reaction, $CO + H_2O \rightarrow CO_2 + H_2$, is also included in both fuel channels and porous anode using a reaction rate described by the Arrhenius law [20]. For all electrochemical reacting flow simulations in this study, we keep Re fixed with $Re_{anode} = 100$ and $Re_{cathode} = 300$.

4. Results and discussion

4.1. Velocity distributions in a porous rib-channel

Fig. 4a presents four sets of normalized gaseous velocity distributions measured in a porous rectangular rib-channel with four different values of ε varying from 0 to 0.43 (different symbols) at $Re = 100$ using PIV, where $U_c(\varepsilon = 0)$ is the centerline velocity of the rib-channel at $\varepsilon = 0$ and h is the rib-channel height above the porous media. For clarity, only two sets of numerical data at $\varepsilon = 0$ and $\varepsilon = 0.43$ (dash lines) using the assumption of $\mu_e = \mu_f$ in the Brinkman equation are included in Fig. 4a for comparison. Since the present porous media are not optically accessed, PIV measurements can only be performed above the porous interface. Moreover, the image processing very near the porous interface ($y/h < 0.025$) may suffer higher experimental uncertainties due to the light scattering from the surface and thus PIV data below $y/h = 0.025$ will not be presented in Fig. 4a. For the case of $\varepsilon = 0$, numerical flow data are in a very good agreement with experimental PIV data. But for the case of $\varepsilon = 0.43$, numerical flow data close to the porous interface ($y/h < 0.1$) are found to be smaller than the available experimental data. This is because the assumption of $\mu_e = \mu_f$ is used in numerical flow simulations. Taking a close look at velocity profiles near the porous interface from Fig. 4a and b shows the same velocity data within $-0.1 \le y/h \le 0.1$ where $y/h = 0$ is the porous interface. To the first-order approximation, these three PIV data sets at three different values of ε (solid symbols) in Fig. 4b are linearly fitted with their fitting lines extending to the porous interface. This may allow us to estimate the slip velocities ($\hat{U}_{s,exp}$) (open symbols) and corresponding strain rates ($\dot{\gamma}$) at the porous interface. The difference of normalized slip velocities between experimental and numerical data, is $\Delta\hat{U}_s = \hat{U}_{s,exp} - \hat{U}_{s,num}$, as indicated in Fig. 4b. It is found that the higher the value of ε is, the higher the magnitude of $\Delta\hat{U}_s$ (see the inset in Fig. 4b). Applying Eq. (3), the effective viscosity (μ_e) can be estimated by $\mu_e = \mu_f \alpha^2$ [11]. As shown on the inset of Fig. 4b, μ_e is sensitive to ε for which the ratio of μ_e/μ_f increases from 10^{-4} to 4.9×10^{-3} when ε increases from 0.04 to 0.43. These results show that the assumption of $\mu_e = \mu_f$ commonly used in the Brinkman equation for numerical simulations of SOFCs cannot predict correctly the momentum transport in the porous media when $0 < \varepsilon \le 0.43$, because the actual slip velocities at the porous interface are underestimated.

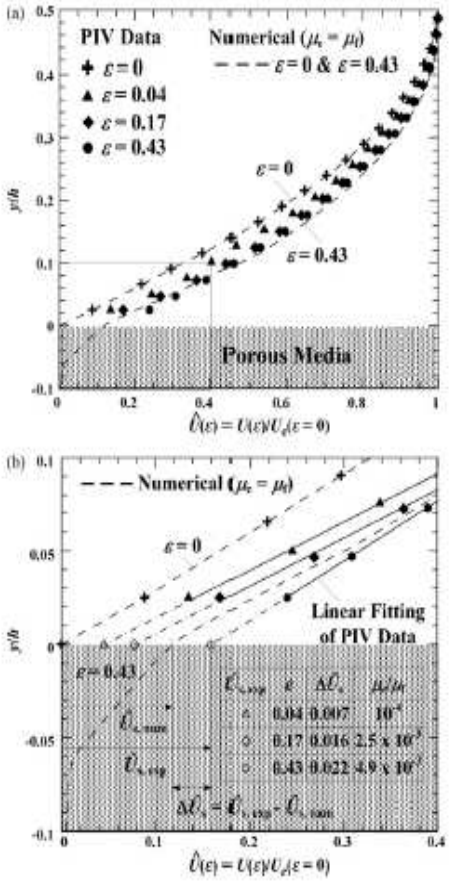

Fig. 4. (a) Four sets of normalized gaseous velocity profiles in a rectangular rib-channel with four different values of ε varying from 0 to 0.43 at $Re = 100$ measured by PIV. For clarity, only two sets of numerical data at $\varepsilon = 0$ and $\varepsilon = 0.43$ using the assumption of $\mu_e = \mu_f$ in the Brinkman equation are included for comparison. (b) Same data as (a), but only for velocity profiles near the porous interface showing the estimation of $\hat{U}_{s,exp}$ using the linear fitting. The inset table lists corresponding values of ε, $\Delta\hat{U}_s$, and μ_e/μ_f estimated from PIV data.

4.2. Effect of μ_e/μ_f on cell performance

So μ_e is not equivalent to μ_f and it is several orders in magnitude smaller than μ_f. It is thus important to know the influence of such difference between μ_e and μ_f in the Brinkman equation to the cell performance. Currently, this influence can be only studied by numerical simulations. Applying the same single-unit cell stack model described in Section 3 with two drastically different values of μ_e/μ_f while keeping all the other conditions fixed, Fig. 5 shows two data sets of corresponding voltage and power density as a function of current density, where the same values of $\varepsilon = 0.3$, $k = 10^{-11}\ m^2$, $\tau = 1.5$, $Re_{anode} = 100$, and $Re_{cathode} = 300$ are used in the model. It is found that the value of peak power density (PPD = 531 mW cm^{-2}) occurring at 818 mA cm^{-2} for $\mu_e/\mu_f = 4.9 \times 10^{-3}$ is nearly 11% higher than that of $\mu_e/\mu_f = 1$ (PPD = 475 mW cm^{-2} at 731 mA cm^{-2}). Clearly, this increase in the value of PPD up to 11% indicates that the effect of μ_e/μ_f plays a role on the cell performance and thus cannot be neglected.

Since our experimental data reveal that the ratio of μ_e/μ_f varies with ε, we thus perform sensitivity analyses of the ratio of μ_e/μ_f to

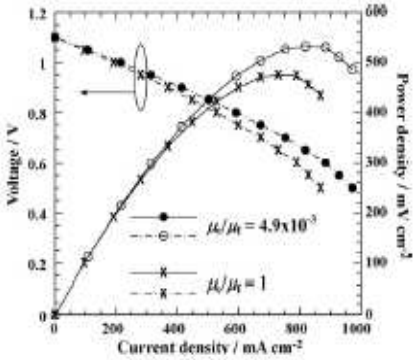

Fig. 5. Comparison of power-generating characteristics when two different values of μ_e/μ_f are used in the same single-unit cell stack model with fixed values of $\varepsilon = 0.3$, $k = 10^{-11}$ m^2, $\tau = 1.5$, $Re_{anode} = 100$, and $Re_{cathode} = 300$.

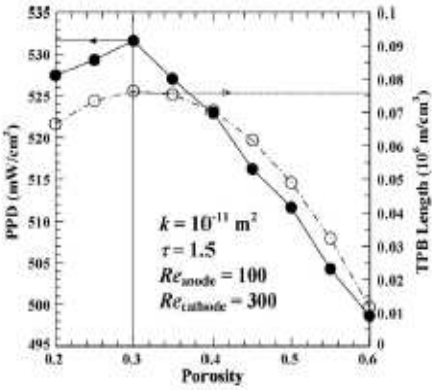

Fig. 7. Peak power density and TPB length as a function of ε.

the peak power density of the single-unit cell stack at three different values of ε. These results are presented in Fig. 6 showing three points. First, for all three different values of ε, values of PPD increase from about 470 mW cm^{-2} to about 520 mW cm^{-2} when the ratio of μ_e/μ_f decreases from 1 to 0.1. Secondly, further decreasing of μ_e/μ_f from 0.1 to 0.01 results in only a little increase of PPD and then values of PPD remain constant when $\mu_e/\mu_f \le 0.005$. Thirdly, values of PPD at $\varepsilon = 0.3$ are found to be higher than those at $\varepsilon = 0.2$ and at $\varepsilon = 0.4$ showing the effect of ε on the power density. These results may be understood from the governing equations used in numerical simulations. For instance, the additional second-order body force term ($\varepsilon\mu_e\nabla^2\vec{U}$) in the Brinkman equation involving the effective viscosity which is the last term of Eq. (5) should act as a drag force imposed by the boundaries of the grains in porous electrodes. When the Brinkman equation with the assumption of $\mu_e/\mu_f = 1$ is used, such drag force as the resistance to flow will be overestimated resulting in a decrease of the amount of the reactant that could penetrate into the triple-phase-boundary (TPB) around the reaction sites. But when μ_e/μ_f is sufficiently small ($\mu_e/\mu_f < 0.01$) as suggested by the present sensitivity analysis (Fig. 6), the drag force term, $\varepsilon\mu_e\nabla^2\vec{U}$, becomes insignificant and the mass transport in porous electrodes should be dominated by the Knudsen diffusion and/or the molecular diffusion. This may explain why the value of PPD obtained at $\mu_e/\mu_f = 4.9\times10^{-3}$ can be 11% higher than that when using $\mu_e/\mu_f = 1$ (see Fig. 5).

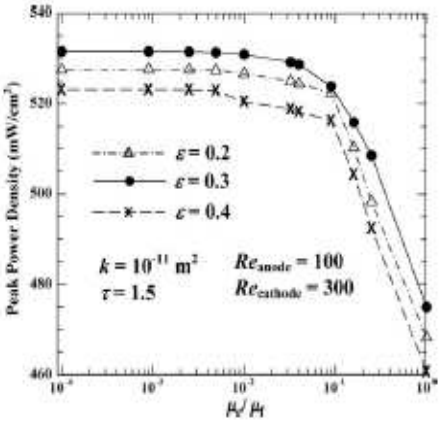

Fig. 6. Variations of peak power density with μ_e/μ_f at three different values of ε.

Can the present measured values of μ_e/μ_f be applicable when different anode materials and/or different cell configurations (anode-supported vs. electrolyte-supported or planar-type vs. tubular-type) are used? The answer is yes, because the present PIV measurements consider only fluid dynamics aspects for porous flows with an emphasis on the effect of porosity. Hence, the present PIV results should be valid even for real applications as long as the porosity of the material is fixed. However, real applications are very complex, because the electrochemical reactions might change the porosity of the electrodes. For instances, the chromium poisoning and the carbon deposition may reduce the porosity of electrodes. For cases with changing porosity, the present PIV data obtained at fixed values of porosity must be viewed with caution. In this study, we only consider constant values of porosity and thus we shall use measured transport properties, as shown on the inset table of Fig. 4, for further numerical studies.

4.3. Effects of ε, k and τ on cell performance

In attempt to predict an optimal combination of anodic microstructures for planar anode-supported SOFCs, we perform sensitivity tests on effects of ε, k, and τ to the cell performance using 3D single-unit cell stack model with measured porous transport properties. In it only one variable is changed at a time while keeping the other variables constant. At fixed values of $k = 10^{-11}$ m^2 and $\tau = 1.5$, Fig. 7 presents the effect of ε on the cell performance. It is found that the maximum PPD = 531 mW cm^{-2} occurs at $\varepsilon = 0.3$. Also plotted in Fig. 7 is the variation of the TPB length with ε, where the TPB length is calculated using the formula proposed by Deng and Petric [3]. As can be seen, the increasing and decreasing trends for both PPD and TPB length are essentially the same of which their maximum values all occur at $\varepsilon = 0.3$. On the one hand, it is known that smaller values of anodic ε may provide more reaction sites in anode which may result in higher values of PPD. On the other hand, too small anodic ε can reduce the mass transport rate due to the decrease of the Knudsen diffusion and the molecular diffusion in anode resulting in lower values of PPD. These two opposite effects may explain why the maximum values of PPD and TPB length occur at $\varepsilon = 0.3$.

Figs. 8 and 9 show the effect of k and the effect of τ on PPD, respectively, each including three different values of ε, where $Re_{anode} = 100$ and $Re_{cathode} = 300$ are used for both cases. At any given values of k and τ, values of PPD at $\varepsilon = 0.3$ are found to be larger than those at either $\varepsilon = 0.2$ or $\varepsilon = 0.4$, similar to the results of Figs. 6 and 7. Results from Fig. 8 show that values of PPD increase slightly with k when 10^{-12} m$^2 < k < 10^{-11}$ m^2 and then little increase

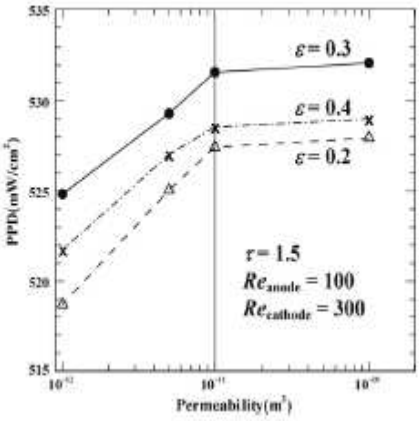

Fig. 8. Variations of peak power density with the anodic permeability at three different values of ε.

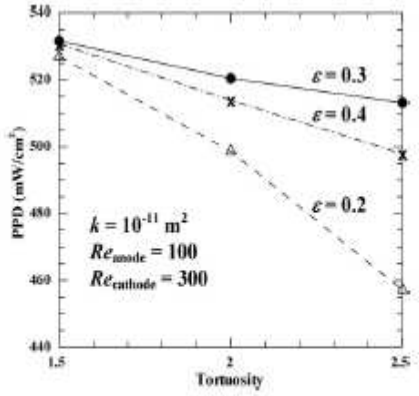

Fig. 9. Variations of peak power density with the anodic tortuosity at three different values of ε.

of PPD is found when $10^{-11}\ m^2 < k < 10^{-10}\ m^2$. Porous anodes with larger values of k may enhance the penetration of reactant to have a larger Darcy's velocity resulting in a higher PPD, but their mechanical strength is weakened. Since the TPB length and thus the effect of ε have much stronger influence on the cell performance (Fig. 7) than the effect of k, the appropriate value of $k \approx 10^{-11}\ m^2$ is suggested for the anode-supported SOFCs. Concerning the effect τ, we found that values of PPD increase with decreasing τ. It is known that the ohmic polarization may be increased with increasing τ because of the increase of transport paths for ions and electrons in anode. Furthermore, the anode with larger values of τ would inhibit the exchange of H_2O and H_2 and thus increase the concentration polarization, suggesting that the value of τ for the anode should be as small as possible. But $\tau < 1.5$ is considered not practical for real anodic microstructures [2]. In addition, the effect of τ is more significant in the dense anode (smaller ε), as can be seen from Fig. 9, in which a 13% increase of PPD can be found when values of τ decrease from 2.5 to 1.5 with $\varepsilon = 0.2$ while only 3% increase of PPD is found at $\varepsilon = 0.3$. To this end, these results suggest that a combination of $\varepsilon = 0.3$, $k = 10^{-11}\ m^2$, and $\tau = 1.5$ used in anodic microstructures can achieve the highest PPD.

5. Conclusions

This study aims to predict optimal anodic microstructures for planar anode-supported SOFCs using 3D electrochemical flow model with measured porous transport properties. Two key points are summarized below.

(1) A transparent porous rib-channel with different values of ε varying from 0 to 0.43 is applied to measure an effective viscosity (μ_e) in the Brinkman equation commonly used to predict flow properties in porous electrodes using PIV. It is found that, contrary to the popular scenario, μ_e is not equal to the fluid viscosity (μ_f), but it is several orders in magnitude smaller than μ_f which can result in more than 10% difference on the cell's power density.
(2) Numerical sensitivity analyses based on a single-unit cell stack model found that while keeping k and τ fixed with ε varying from 0.2 to 0.6, the highest PPD occurs at $\varepsilon = 0.3$ where the corresponding triple-phase-boundary length is a maximum. An optimal combination of $\varepsilon = 0.3$, $k = 10^{-11}\ m^2$, and $\tau = 1.5$ for anodic microstructures is suggested to achieve higher cell performance.

These results should be useful for further improvement of the cell performance of planar SOFCs.

Acknowledgements

This work is financially supported by the Institute of Nuclear Energy Research (972001INER036) in Taiwan. The authors wish to thank the National Center for High-performance Computing for computer time and facilities.

Appendix A. Supplementary data

Supplementary data associated with this article can be found, in the online version, at doi:10.1016/j.jpowsour.2009.10.048.

References

[1] S.C. Singhal, K. Kendall, High-temperature Solid Oxide Fuel Cells: Fundamentals, Design and Applications, Elsevier Ltd., Kidlington, 2003.
[2] A.V. Virkar, J. Chen, C.W. Tanner, J.W. Kim, Solid State Ionics 131 (2000) 189–198.
[3] X. Deng, A. Petric, J. Power Sources 140 (2005) 297–303.
[4] M. Ni, M.K.H. Leung, D.Y.C. Leung, Energy Convers. Manag. 48 (2007) 1525–1535.
[5] H. Fukunaga, M. Ihara, K. Sakaki, K. Yamada, Solid State Ionics 86–88 (1996) 1179–1185.
[6] E. Hernandez-Racheco, D. Singh, P.N. Hutton, N. Patel, M.D. Mann, J. Power Sources 138 (2004) 174–186.
[7] S.H. Chan, Z.T. Xia, J. Appl. Electrochem. 32 (2002) 339–347.
[8] J. Bear, Dynamics of Fluids in Porous Media, Dover Publications, New York, 1988.
[9] H.C. Brinkman, Appl. Sci. Res. A1 (1947) 27–34.
[10] G.S. Beavers, D.D. Joseph, J. Fluid Mech. 30 (1967) 197–207.
[11] G. Neal, W. Nader, J. Chem. Eng. 52 (1974) 475–478.
[12] R.C. Givler, S.A. Altobelli, J. Fluid Mech. 258 (1994) 355–370.
[13] P. Dokmaingam, S. Assabumrungrat, A. Soottitantawat, I. Sramala, N. Laosiripojana, Int. J. Hydrogen Energy 34 (2009) 410–421.
[14] D. Cui, L. Liu, Y. Dong, M. Cheng, J. Power Sources 174 (2007) 246–254.
[15] G. Wang, Y. Yang, H. Zhang, W. Xia, J. Power Sources 167 (2007) 398–405.
[16] C.M. Huang, S.S. Shy, C.H. Lee, J. Power Sources 183 (2008) 205–213.
[17] A. Koponen, M. Kataja, J. Timonen, Phys. Rev. E 54 (1996) 406–410.
[18] T.S. Yang, S.S. Shy, J. Fluid Mech. 526 (2005) 171–216.
[19] CFD-RC, CFD-ACE+ User Manual, CFD-RC, Huntsville, USA, 2003, http://www.cfdrc.com.
[20] J.M. Klein, Y. Bultel, S. Georges, M. Pons, Chem. Eng. Sci. 62 (2007) 1636–1649.

Journal of Power Sources 195 (2010) 6280–6286

Contents lists available at ScienceDirect

Journal of Power Sources

journal homepage: www.elsevier.com/locate/jpowsour

The impact of flow distributors on the performance of planar solid oxide fuel cell

C.M. Huang[a], S.S. Shy[a,b,*], H.H. Li[a], C.H. Lee[c]

[a] Department of Mechanical Engineering, National Central University, 300 Jhong-da Road, Jhong-li, Tao-yuan 32001, Taiwan
[b] Center for Energy Research, College of Engineering, National Central University, Taiwan
[c] Institute of Nuclear Energy Research, Lung-tan, Tao-yuan 32546, Taiwan

ARTICLE INFO

Article history:
Received 25 February 2010
Received in revised form 22 April 2010
Accepted 22 April 2010
Available online 18 May 2010

Keywords:
Planar solid oxide fuel cell
Single-cell stack test
Flow distributors
Flow uniformity
Cell performance measurements
Anodic re-oxidation

ABSTRACT

This paper presents a newly established testing rig for planar solid oxide fuel cell. Two sets of nearly identical single-cell stacks except using different designs of flow distributors are measured to show how exactly the cell performance of such single-cell stacks would vary with a change in the degree of flow uniformity. It is found that by using small guide vanes around the feed header of commonly used rib-channel flow distributors to improve effectively the degree of flow uniformity, the power density of the single-cell stack can be increased by 10% as compared to that without using guide vanes under exactly the same experimental conditions. Also discussed are the start-up procedure and effects of hydrogen and air flow rates varying from 0.4 slpm to 1 slpm on cell performance of these two single-cell stacks which are measured over a range of the operating temperature varying from 650 °C to 850 °C. After 100 h of continuous cell operation, the examination of the reduction and oxidation stability of the anodic surface reveals that the improvement of flow uniformity in flow distributors is useful to achieve a more balanced use of the anodic catalyst.

1. Introduction

The planar solid oxide fuel cell (SOFC) is of great interest because of its fuel flexibility, compactness, and potential for achieving very high power density [1]. A typical planar SOFC is assembled by the positive electrode–electrolyte–negative electrode (PEN) and the current collectors on both anode and cathode sides that are sandwiched by a pair of interconnects or flow distributors. Nowadays, many different designs of interconnects or flow distributors with straight flow channels separated by rectangular ribs have been used to distribute the fuel and the oxidant gases to the PEN surface, see for instances Refs. [2,3] among many others. A typical flow pathway of interconnects in planar SOFCs may include three parts from a feed header and multi-flow channels to an exhaust header. Furthermore, a good design of flow distributors not only can distribute the fuel and the air uniformly onto the anode and the cathode for achieving uniform diffusion processes through porous electrodes, but also can provide sufficient air flow on the cathode for removing possible hot spots during the long-term cell operation. Thus, the optimization of interconnects or flow distributors is crucial for further improvement of the cell performance of planar SOFC [4,5].

Recently, Shy and co-workers [6] found that flow uniformity in rib-channel interconnects may play a role on the cell performance of a single-cell stack based on 3D numerical models. Note that these numerical flow results in Ref. [6] have been validated by experimental flow data measured by a hydraulic platform. In Ref. [6], four different designs of flow distributors with the same 12 rectangular flow channels divided by 11 ribs were investigated, as schematically shown in Fig. 1a. These four designs were respectively (1) a single-inlet/single-outlet design proposed by Yakabe et al. [7], (2) a double-inlet/single-outlet design by de Haart et al. [8], (3) same as (2) but with an extended rib in the center dividing symmetrically these 12 flow channels into two portions, and (4) same as (2) but with 10 small guide vanes equally spaced in the feed header. A flow uniformity coefficient,

$$\Gamma = \left\{1 - \left[\frac{1}{n}\sum_{i=1}^{n}\left(\frac{u_i - \bar{u}}{\bar{u}}\right)^2\right]^{0.5}\right\} \times 100\%,$$

proposed by Huang et al. [6], was used to indicate the degree of flow uniformity for these aforementioned designs of interconnects, where $n = 12$ representing the total number of rib-channels, u_i the flow velocity in the ith rib-channel, and $\bar{u}$ the averaged mean velocity. Both flow simulations and measurements showed that the design (4) using simple guide vanes in the feed header can significantly improve the flow uniformity and thus can provide the most uniform flow distribution among these four different designs [6].

* Corresponding author at: Department of Mechanical Engineering, National Central University, 300 Jhong-da Road, Jhong-li, Tao-yuan 32001, Taiwan.
Tel.: +886 3 426 7327; fax: +886 3 427 6157.
E-mail address: sshy@ncu.edu.tw (S.S. Shy).

0378-7753/$ – see front matter © 2010 Elsevier B.V. All rights reserved.
doi:10.1016/j.jpowsour.2010.04.073

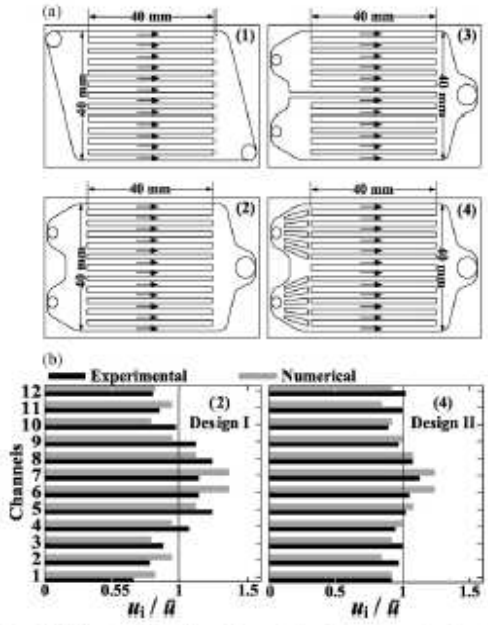

Fig. 1. (a) Schematics of four different designs of flow distributors previously used in numerical studies [6]. (b) Comparisons of experimental and numerical velocity distributions in 12 rib-channels for designs (2) and (4) (here denoted as designs I and II), where $\bar{u}$ was the mean velocity averaged from the velocity data in 12 rib-channels. These velocity data were extracted from Fig. 6 in Ref. [6].

For completeness, flow velocity distributions in each of these 12 rib-channels for the designs (2) and (4) are presented in Fig. 1b, both including experimental and numerical data extracted from Fig. 6 of Ref. [6]. Note that here we denote these two previous designs (2) and (4) as the designs (I) and (II). It can be seen that by using simple small guide vanes evenly spaced in the feed header (design II), the degree of flow uniformity can be significantly improved where the value of I' is greater than 90% as compared to that of design I without using small guide vanes where $I' \approx 80\%$. More important, such improvement on the degree of flow uniformity can result in an increase of the peak power density (PPD) up to 11% as suggested in Ref. [6] based on 3D numerical models. This motivates the present work aiming to address the following question. How exactly would the effect of flow uniformity vary with a change in the power density of single-cell stacks using different designs of flow distributors? Hence, this paper introduces a high-temperature SOFC testing rig to measure the cell performance for these aforementioned single-cell stacks. By comparing the power-generating characteristics between two sets of nearly identical single-cell stacks except that different designs of flow distributors (designs I and II) having different degrees of flow uniformity are applied, the influence of flow uniformity to cell performance can be thus measured. However, there are some problems to be solved before a clear-cut result on the effect of flow uniformity can be obtained, as discussed below.

At high-temperature conditions, the commonly used metallic interconnects using the materials such as the chromium-based (Cr) alloy with a higher oxidant resistance (e.g. crofer 22-APU) and the doped $LaCrO_3$-based ceramics have higher values of the coefficient of thermal expansion (CTE) than that of the PEN, resulting in high thermal stresses and probably causing cracks of the PEN [9]. Furthermore, the Cr-based vapor species volatilized from these metallic interconnects can be oxidized and deposited on the cathode, which in turn inhibit the reduction of oxygen when the operating temperature is higher than 800 °C [10]. Both the mismatch of CTE among components and the Cr-poisoning problems can lead to rapid cell degradation [11]. To circumvent the aforementioned problems, Liu et al. [12] established a single-cell stack using a disc-shape PEN. In Ref. [12], the gaseous reactants were distributed via various pin-type ceramic flow distributors and the current on the surface of electrodes was directly collected by Ni (anode) or Pt (cathode) meshes, so that the Cr-poisoning problem from the metallic interconnects can be avoided. In addition, the single-cell stack was assembled using a seal-less arrangement and thus the CTE matching problem among various components can be also avoided [12]. It should be noted that such a seal-less assembly could have a serious problem on the cell degradation due to the cross-leakages of fuel and air in the single-cell stack. This leakage problem must be solved before any practical use. Therefore, this study applies the similar methodology proposed by Liu et al. [12] using ceramic rib-channel flow distributors and the seal-less assembly for the present square-shape single-cell stack test, where the currents on the surface of electrodes are collected by using Ni and Pt meshes for the anode and the cathode, respectively. Further, we keep the flow rate of the anode being at least equal to or slightly higher than that of the cathode to avoid the possible air leakage to the anode when the seal-less assembly is used.

In the following sections, we will first introduce the single-cell stack testing rig. Next we will describe the start-up procedure and show the time dependence of the open circuit voltage (OCV) for the present two sets of nearly identical single-cell stacks except using different designs of flow distributors. Results of power-generating characteristics are then presented to demonstrate how exactly the cell performance of these two sets of single-cell stacks would vary with a change in the degree of flow uniformity. Variations of operating temperatures and hydrogen and air flow rates to the cell performance of the single-cell stacks are also discussed. Finally, we will show the observation of the re-oxidation zone on the anodic surface of the PEN after 100 h of the continuous cell operation that occurs only in the case using the design I.

2. A single-cell stack testing rig

Fig. 2 shows photographs of a SOFC testing platform using a temperature-controlled furnace where the single-cell stack is tested. Also shown in Fig. 2 are various gas supply lines, the humidifier, the flow controller, the monitoring and measuring system (a Prodigit 3310D electronic load controlled by a data acquisition computer), and an exhaust gas hood. The furnace can provide an isothermal environment from room temperature to 1000 °C. Thus, the current–voltage (I–V) and current–power (I–P) characteristics of the single-cell stack can be measured at the selected high-temperature conditions.

The left part of Fig. 3 presents a photograph of the arrangement of the testing single-cell stack embedded in a ceramic housing inside a furnace, whereas the right part shows the exploding sketch of such a single-cell stack. As can be seen, the single-cell stack consists of an anode-supported PEN with an effective area of 40 mm × 40 mm (ASC 3 purchased from H.C. Starck), a crofer 22-APU supporting frame, and two current collectors using a porous nickel sponge on the anode side and a platinum mesh on the cathode side for the collection of the electrode current. The use of the metallic frame not only provides the mechanical support to the PEN but also features as a separator to prevent the possible cross-leakages between fuel and oxidant from both feed and

Fig. 2. A SOFC testing platform including a furnace in which the single-cell stack is tested, various gas supply valves and lines, the exhaust gas hood, and power measuring devices.

exhaust headers. In this study, both upper and lower flow distributors (see Fig. 3) are fabricated by aluminum oxide materials, so that the poisoning problem of the electrodes due to the chromium volatilization from the metallic flow distributors can be avoided. The PEN, the frame, and the current collectors are then sandwiched by the upper and lower flow distributors. After many tests, appropriate load plates having a total of 3 kg are applied (see the left part of Fig. 3) in order to obtain a good electrical contact among the PEN and the two current collectors. Note that no bolts are used for the assembly of the present seal-less single-cell stack. So the stack is not tightly screwed and thus the CTE matching problem among different components of the stack can be eliminated. The above arrangements are essential to simplify the very complex poisoning and CTE matching problems occurred in the real SOFC operation and thus allow a clear-cut measurement purely on the effect of flow uniformity to the cell performance to be achieved. By direct comparing power-generating characteristics between two sets of nearly identical single-cell stacks except using different designs of flow distributors, one with small guide vanes around the feed header having higher flow uniformity (design II) and the other without (design I), we are able to identify the actual influence of flow uniformity to the cell performance.

3. The start-up procedure

The standardization of the testing procedure is crucial to obtain repeatable and reliable experimental data and thus must be taken with great caution. This study follows the same testing procedure proposed by Haanappel and Smith [13] for cell performance measurements of these aforementioned single-cell stacks using

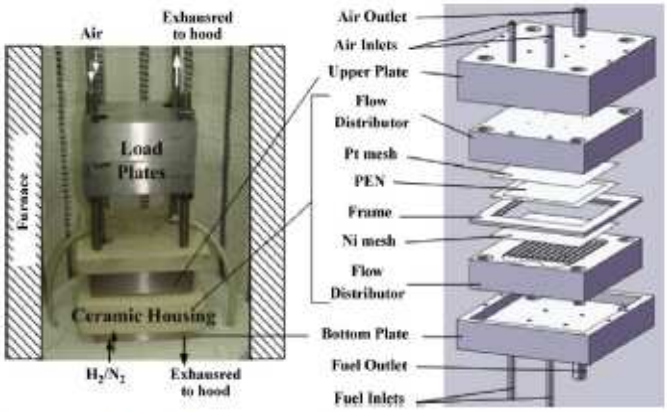

Fig. 3. The arrangement of a testing single-cell stack positioned inside a ceramic housing in the furnace with appropriate loading plates along with the exploding sketch of the single-cell stack.

two different designs of flow distributors. As can be found in Ref. [13], the procedure begins by delivering the test plan and identifying the critical parameters for the cell tests. Following that the single-cell stack is properly mounted to the testing platform for pre-conditioning of the single-cell stack. Then the very slow heating process of the single-cell stack is carried out under nitrogen, cathode and anode sides, respectively, with gas flow rates of 0.2 standard liters per minute (slpm) on both sides [13]. In this study, a programmable logic controller is used to control the temperature of the furnace, such that both heating and cooling rates of the furnace can be controlled at a constant rate of 1 °C min^{-1} in order to very slowly heat up and/or cool down the furnace to the wanted temperature. As pointed out by Haanappel et al. [14], the lower reduction temperature of the anodic catalyst can result in a lower cell performance having a longer time to reach steady state performance and a much larger scattering of data points. Therefore, for achieving a higher cell performance, this study uses a high reduction temperature at T = 850 °C during the 24-h anode reduction process, in which mixtures of hydrogen and nitrogen with the flow rates of Q_{H_2} = 0.08 slpm and Q_{N_2} = 0.2 slpm are continuously provided to the anode together with an air flow rate of Q_{air} = 0.08 slpm to the cathode.

Fig. 4 shows the entire time dependence of the cell voltage during the start-up process for two independent sets of nearly identical single-cell stacks except that their flow distributors are different, one with small guide vanes (design II) while the other without (design I). Note that the time origin in Fig. 4 is selected at the time when the very slowly heated single-cell stacks have reached the wanted temperature at T = 850 °C. It is found that values of OCV are essentially the same for both designs only in the very beginning of the start-up process. As the anode reduction time increases further up to 2 h, the value of OCV for the design II quickly increases and approaches its maximum value of about 1.15 V. This time period is much faster than that of the design I which needs more than 9 h of the anode reduction time to reach its maximum OCV value. The reason for such a discrepancy in the time dependence of values of OCV between these two cases is clearly due to the influence of flow uniformity, since almost all experimental conditions used in these two sets of single-cell stacks are the same except that the design II using small guide vanes around the feed header of the rib-channel flow distributor has a higher flow uniformity than that of the design I. From the time variation of the cell voltage during the start-up process (Fig. 4), we conclude that a more uniform reduction of the anodic catalyst can be obtained by improving the flow uniformity in rib-channel flow distributors.

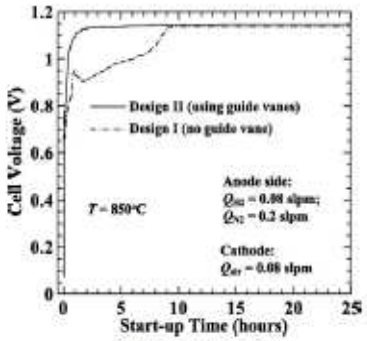

Fig. 4. Variations of OCV during the start-up process for the two sets of identical single-cell stacks except using different flow distributors.

4. Power-generating characteristics

After the completion of the start-up process while keeping the operating temperature constant at T = 850 °C, we measure individually the power-generating characteristics of the aforementioned two single-cell stacks using different designs of flow distributors (designs I and II). For both designs, the measurement begins from the zero current for the OCV and then increases the current density load incrementally, each increment by 12.5 mA cm^{-2}, until that the current density load is increased to be 400 mA cm^{-2}. Furthermore, the measuring time period for each data point should be long enough to assure that the power-generating data are obtained at the equilibrium state. By systematically testing different measuring time periods varying from 0.5 s to 50 s, we found a suitable measuring time period of 30 s that can meet the equilibrium requirement and thus it is used for all measurements in this study. Note that the cell voltage at every incremental step of increasing the current density load is repeatedly measured 30 times to obtain a correct statistical average value. These results are presented and discussed below.

4.1. Effect of flow uniformity at various hydrogen flow rates

Under exactly the same experimental conditions except using or not using 10 small guide vanes in the feed header of flow distributors (see Fig. 1), we measure the I–V and I–P curves for each of two sets of single-cell stacks at four different hydrogen flow rates while keeping $Q_{H_2} = Q_{air}$ and the operating temperature constant at T = 850 °C. These results are presented in Fig. 5, where corresponding values of the power density are also plotted. Our experimental data show that for the case of using small guide vanes (design II), the overall cell performance is found to be generally better than the case without using small guide vanes (design I) and this is valid for all flow rates studied varying from 0.4 slpm to 1.0 slpm. Obviously, such a better cell performance obtained for the design II is due to the usage of small guide vanes that can improve effectively the degree of flow uniformity in rib-channel flow distributors. The higher flow uniformity is, the higher power density is. As seen from Fig. 5a for the case of the lower Q_{H_2} = 0.4 slpm, a weak concentration polarization can be observed when the voltage is below 0.7 V. However, for higher hydrogen flow rates (Figs. 5b–d), no sign of the concentration polarization can be observed when the maximum current density load is limited at 400 mA cm^{-2}.

To better demonstrate the effect of flow uniformity to the cell performance, the power density data measured at the maximum current density load (I_d = 400 mA cm^{-2}) for both designs I and II (see Fig. 5) are re-plotted against the hydrogen flow rate. These results are presented in Fig. 6. It is found that at the fixed operating temperature of T = 850 °C, values of the power density, respectively for the design II and/or the design I, increase largely from 259 and/or 232 mW cm^{-2} to 295 and/or 274 mW cm^{-2} when the hydrogen flow rate increases from 0.4 slpm to 0.6 slpm. This result shows that the power density is sensitive to the hydrogen flow rate when $Q_{H_2} \leq 0.6$ slpm. On the other hand, at higher values of Q_{H_2} = 0.8 and 1.0 slpm, the power density is found to be not so sensitive to the increase of Q_{H_2}, where the design II has a power density of 311 mW cm^{-2} compared to 280 mW cm^{-2} for the design I at the same Q_{H_2} = 1.0 slpm. It is worthy noting that by using simple small guide vanes around the feed header of the rib-channel flow distributor (design II) to improve effectively the degree of flow uniformity, the power density of the single-cell stack can be increased by about 10% as compared to that without using guide vanes (design I) under exactly the same experimental conditions (see Fig. 6).

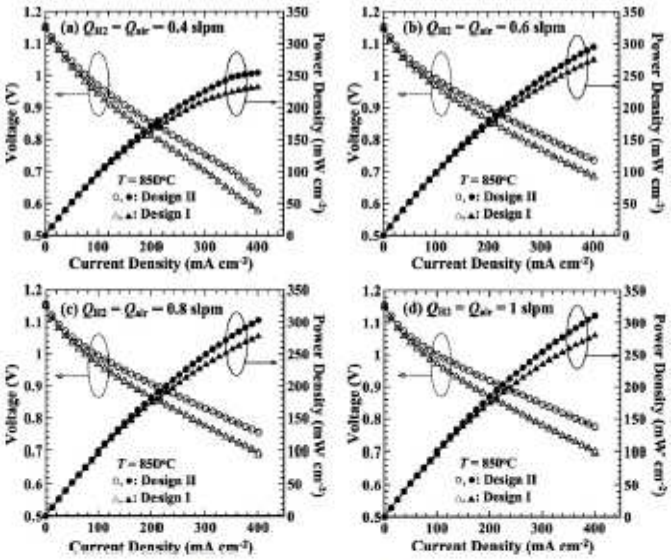

Fig. 5. Comparison of power-generating characteristics between two sets of the single-cell stack using different designs of flow distributors over a range of Q_{H_2} and Q_{air} varying from 0.4 slpm to 1 slpm at a constant operating temperature $T = 850$ °C.

4.2. Effect of flow uniformity at various operating temperatures

Using the similar arrangement as Fig. 6 for both designs I and II, Fig. 7 presents the comparison of power-generating characteristics between these two single-cell stacks at three different operating temperatures: (a) $T = 650$ °C, (b) $T = 750$ °C, and (c) $T = 850$ °C, respectively, where the flow rates are kept constant at $Q_{H_2} = Q_{air} = 1.0$ slpm. As can be seen from Fig. 7, values of OCV are about 1.17 V, 1.16 V, and 1.15 V respectively at $T = 650$ °C, 750 °C, and 850 °C, of which a small decrease of OCV with increasing the operating temperature is found. This is expected because the Gibbs free energy of reactants decreases with increasing temperature. When the operating temperature is low at $T = 650$ °C, the increase of the power density due to the influence of flow uniformity is only incremental, where the measurement is ended at 0.56 V (Fig. 7a). As T increases, the cell performance for both designs quickly increases because the ionic and electrical conductivities of the cell components increase with the operating temperature. It is found that there is an increase of 11.1% in the value of the power density when compared the design II with the design I at the same $T = 850$ °C and $I_d = 400$ mA cm^{-2} (see Fig. 7c). Such an increase in the power density is due to the fact that the higher flow uniformity in flow distributors results in a more uniform use of the anodic catalyst.

Fig. 8 shows the same power density data measured at 0.8 V from Fig. 7, but plotted against the operating temperature. It is clear that the power density of the design II is very sensitive to the operating temperature, as its value increases from 100 mW cm^{-2} to about 300 mW cm^{-2}, a nearly three-fold increase, when values of T increase from 650 °C to 850 °C. Similar results are also found for the design I. Moreover, the higher the operating temperature is, the larger the influence of flow uniformity is, as can be seen from Fig. 8.

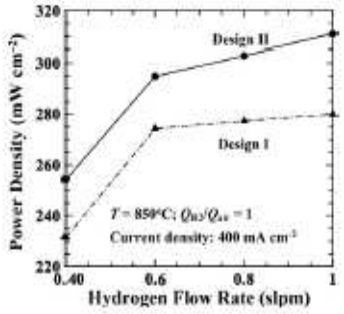

Fig. 6. Effect of hydrogen flow rate on the power density for two sets of identical single-cell stacks except using different flow distributors, where the operating conditions are fixed at $T = 850$ °C, $Q_{H_2}/Q_{air} = 1$, and the current density $I_d = 400$ mA cm^{-2}.

4.3. Observation of anodic re-oxidation zone

Fig. 9a and b presents photographs of two different designs of double-inlet/single-outlet rib-channel flow distributors, respectively the design I and the design II that are used in the aforementioned single-cell stack testing, along with their associated anodic and cathodic surfaces of the PENs after 100 h of the continuous operation. Note that the only difference between these two flow distributors (see Fig. 9) lies in the use of 10 small guide vanes around the feed header for the design II featuring a much higher degree of flow uniformity than that of the design I. Both flow distributors have eight small holes on their rib-channel area allowing the access of the voltage and current probes for power measurements. As seen from Fig. 9a for the design I, different color distributions on the anodic surface of the PEN are observed as marked by white dashed lines, indicating that the anodic catalyst may suffer the formation of anodic re-oxidation zone. This is

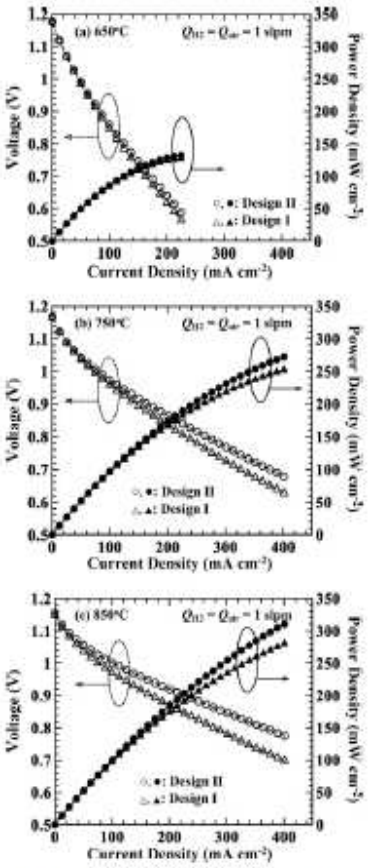

Fig. 7. Comparison of power-generating characteristics between two sets of the single-cell stack using different designs of flow distributors operated at three different temperatures: (a) T = 650 °C, (b) T = 750 °C and (c) T = 850 °C.

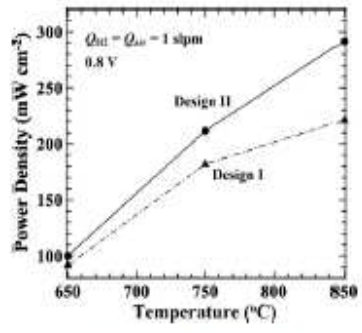

Fig. 8. Effect of operating temperatures on the power density for two sets of identical single-cell stacks except using different flow distributors, in which the comparison is made at the same 0.8 V with $Q_{H_2} = Q_{air}$ = 1 slpm.

not due to the air leakage because we have carefully controlled the same flow rates applied for both anode and cathode, and more importantly, the obtained values of OCV are all greater than 1.1 V. In addition, this is not just a one-shot phenomenon, because such an anodic re-oxidation zone is observed for all cases using the design I as their flow distributors after 100 h of cell operation. Previous results applying the scanning electron microscope (SEM) technique have showed that the color of an initial anode (NiO/YSZ) with a stoichiometric ratio between Ni and O elements should be in green, the color of a fully-reduced anode (metallic Ni/YSZ) should be in grey, and the color of a re-oxidized anode ($Ni_{1-\delta}O$/YSZ) should change from green to black (dark green) with increasing δ, as can be found in Ref. [15]. In Fig. 9a, all three colors (green, dark green, and grey) are observed from the anodic surface for the design I. In other words, different composites of the anodic catalyst for the design I have been formed after a long time operation (100 h), on which there are the fully-reduced area (grey color), the local re-oxidized zone (dark green), and the still oxidized part (green). Contrary to that of the design I, only one color of the anodic surface of the PEN is observed when the design II is used, as shown in Fig. 9b, revealing a very uniform reduced anode that is in grey color. By comparing these anodic surfaces between designs I and II, it is straightforward to realize why the better flow uniformity in flow distributors can lead to a better cell performance as discussed in Figs. 5 and 7. To the other side, the cathodic surfaces of the PENs for both designs look almost the same after 100 h of the continuous cell operation (see Fig. 9), probably because the oxygen in the cathode has a much slower reaction rate.

What is the reason for causing the aforesaid anodic re-oxidation in the case of non-uniform flow field? The possible answer may be highlighted from previous studies on the anodic re-oxidation mechanisms (e.g., Refs. [16,17]). As suggested by Hatae et al. [16], the spongy anodic microstructure can be generated when Ni was re-oxidized either by O_2 in air or by the oxide ion current. The latter re-oxidation mechanism has been confirmed by a damage study of Ni–YSZ re-oxidation in anode-supported SOFCs, showing the effect of fuel starvation on the anodic re-oxidation by the oxide ion current. Hence, it is thought that the observed re-oxidation phenomenon occurred only in the case of non-uniform flow field is probably due to local fuel starvation resulting in non-uniform electrochemical reactions and thus non-uniform temperature distributions on the anodic active area.

The aforementioned results are important, because the reduction and oxidation (redox) stability of Ni-based anode is a key reliability issue for SOFCs. The occurrence of the unwanted re-oxidation zone on the anodic surface can decrease the porosity of the anode. This in turn inhibits the fuel diffusion process through the porous anode, makes micro cracks at the interface between the anode and the electrolyte possible, and eventually causes the sever degradation of the anodic catalyst. Such an anodic re-oxidation is attributed to non-uniform fuel flow velocities in these 12 rib-channels (design I), because a non-uniform fuel distribution can result in a non-uniform fuel utilization on the anode and a significant drop of the fuel partial pressure, close to zero, may occur locally for some very small fuel flow velocities. That is why the anodic re-oxidation zone does not occur when the design II with a very high degree of flow uniformity is applied. When the local re-oxidation of the anode occurs, the corresponding local part of the Ni-mesh is also oxidized, which in turn insulates the pass way of the electrons from the anode to the current collector resulting in a decrease of the cell performance. Hence, the improvement of flow uniformity in flow distributors is useful to increase the cell performance (see Figs. 5–8), to avoid the unwanted local re-oxidation of the anode, and to extend the longevity of the cell stack (see Fig. 9).

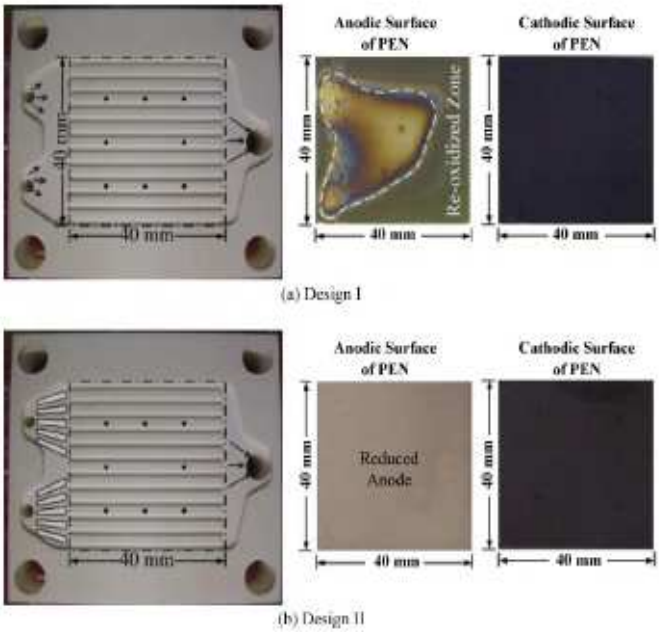

Fig. 9. Two different designs of flow distributors without and/or with guide vanes (designs I and II) and their associated anodic and cathodic surfaces of the PEN after 100 h of operation, showing the influence of flow uniformity on anodic re-oxidation zones occurring only for the case of design I.

5. Conclusions

A high-temperature single-cell stack testing rig for planar SOFC is established to measure the influence of flow uniformity to power-generating characteristics of single-cell stacks over a range of the operating temperature and the hydrogen flow rate. It is found that by simply using small guide vanes equally spaced around the feed header of commonly used rib-channel flow distributors to effectively increase the degree of flow uniformity in flow distributors, the power density of the single-cell stack can be increased by about 10% as compared to that without using guide vanes under exactly the same experimental conditions. Therefore, the present measurement validates our previous numerical predication using the same single-cell stack configuration [6]. Furthermore, the improvement of flow uniformity in flow distributors is helpful to enhance the redox stability of the Ni-based anode, so that a balanced use of the anodic catalyst can be achieved for the continuous cell operation. This is important to extend the longevity of the cell stack.

These results should be useful for planar SOFCs. For further studies, we are currently conducting measurements of resistance spectra of these single-cell stacks using the AC impedance and study the microstructures of the electrodes by SEM in order to understand the cell degradation mechanism and the redox stability of the anode in more depth. These experimental data will be reported in the future.

Acknowledgments

The financial supports from the National Science Council (NSC 97-2212-E-008-085-MY3; 98-2221-E-008-058-MY3; 98-3114-E-008-004) and the Institute of Nuclear Energy Research (972001INER036; 982001INER040) in Taiwan are greatly acknowledged.

References

[1] S.C. Singhal, K. Kendall, High-temperature Solid Oxide Fuel Cells: Fundamentals, Design and Applications, Elsevier Ltd, Kidlington, 2003.
[2] Y. Ji, k. Yuan, J.N. Chung, Y.C. Chen, J. Power Sources 161 (2006) 380–391.
[3] Z. Lin, J.W. Stevenson, M.A. Khaleel, J. Power Sources 117 (2003) 92–97.
[4] T. Ackmann, L.G.J. de Haart, W. Lehert, D. Stolten, J. Electrochem. Soc. 150 (2003) A783–A789.
[5] N. Autissier, D. Larrain, J. Van Herle, D. Favrat, J. Power Sources 131 (2004) 313–319.
[6] C.M. Huang, S.S. Shy, C.H. Lee, J. Power Sources 183 (2008) 205–213.
[7] H. Yakabe, T. Ogiwara, M. Hishinuma, I. Yasuda, J. Power Sources 105 (2001) 144–154.
[8] L.G.J. de Haart, I.C. Vinke, A. Janke, H. Ringel, F. Tietz, in: H. Yokpawa, S.C. Singhal (Eds.), Solid Oxide Fuel Cells (SOFC VII), PV2001-16, The Electrochemical Society Proceedings Series, Pennington, NJ, 2001, p. 111.
[9] A. Selcuk, G. Merere, A. Atkinson, J. Mater. Sci. 36 (2001) 1173–1182.
[10] K. Hilpert, D. Das, M. Miller, D.H. Peck, R. Weiß, J. Electrochem. Soc. 143 (1996) 3642–3647.
[11] H. Tu, U. Stimming, J. Power Sources 127 (2004) 284–293.
[12] H.C. Liu, C.H. Lee, Y.H. Shiu, R.Y. Lee, W.M. Yan, J. Power Sources 167 (2007) 406–412.
[13] V.A.C. Haanappel, M.J. Smith, J. Power Sources 171 (2007) 169–178.
[14] V.A.C. Haanappel, A. Mai, J. Mertens, Solid State Ionics 177 (2006) 2033–2037.
[15] N.M. Tikekar, T.J. Armstrong, A.V. Virkar, J. Electrochem. Soc. 153 (2006) 654–663.
[16] T. Hatae, Y. Matsuzaki, Y. Yamazaki, Solid State Ionics 179 (2008) 274–281.
[17] J. Laurencin, G. Delette, B. Morel, F. Lefebvre-Joud, M. Dupeux, J. Power Sources 192 (2009) 344–352.